Dacarbazine-primed carbon quantum dots coated with breast cancer cell-derived exosomes for improved breast cancer therapy

Pratiksha Tiwari [a,c], Ravi Prakash Shukla [a], Krishna Yadav [a], Neha Singh [a], Disha Marwaha [a], Shalini Gautam [a], Avijit Kumar Bakshi [a], Nikhil Rai [a], Ankit Kumar [a], Deepak Sharma [a], Prabhat Ranjan Mishra [a,b,*]

[a] *Division of Pharmaceutics and Pharmacokinetics, CSIR-Central Drug Research Institute, Lucknow, India*
[b] *Academy of Scientific and Innovation Research (AcSIR), Ghaziabad 201002, U.P., India*
[c] *Jawaharlal Nehru University, New Delhi, India*

A B S T R A C T

Imprecise targeting of chemotherapeutic drugs often leads to severe toxicity during breast cancer therapy. To address this issue, we have devised a strategy to load dacarbazine (DC) into fucose-based carbon quantum dots (CQDs), which are subsequently coated with exosomes (Ex-DC@CQDs) derived from breast cancer cells. Nanoparticle tracking analysis and western blotting revealed that Ex-DC@CQDs retained the structural and functional characteristics of exosomes. We found that exosomes facilitated the transport of DC@CQDs to cancer cells *via* heparan sulfate proteoglycan (HSPG) receptors, followed by an augmented depolarization of the mitochondrial membrane potential, ROS generation, and induction of apoptosis leading to cell death. *In vivo* imaging and pharmacokinetic studies demonstrated enhanced antitumor targeting and efficacy compared to free DC which we attribute to an improved pharmacokinetic profile, a greater tumor accumulation *via* exosome-mediated- HSPG receptor-driven cell uptake, and sustained release of the Ex-DC@CQDs. Our findings may pave the way for the further development of biologically sourced nanocarriers for breast cancer targeting.

1. Introduction

Breast cancer (BC) is a formidable health concern, representing a significant number of cancer-related deaths in women worldwide. Clinical toxicity and targeted imprecision continue to plague BC treatment despite advances in conventional therapies [1,2]. Nanomedicine has introduced Exosomes (Exo) as a promising therapeutic option. These small vesicles (30–150 nm) are secreted by various cells, including cancer cells. Cancer cell-derived Exo can target tumors, promote tissue repair, and modulate the immune system. These Exo also offer several advantages over other drug delivery methods, such as higher bioavailability, enhanced stability, and lower non-targeted cytotoxicity and immunogenicity [3,4]. The selective nature of this delivery mechanism reduces non-specific uptake by healthy cells, minimizing the risk of toxicity and adverse effects. However, the successful development of Exo-based drug delivery systems requires addressing crucial aspects such as *in vivo* biodistribution, pharmacokinetics, and intricate mechanisms of trafficking and communication.

BC cells rely on fucose, a type of sugar, for their growth and division, making them more dependent on it than are normal cells. This dependency on fucose opens up opportunities for targeted therapeutic interventions [5]. CQDs have emerged as a promising delivery platform for selectively targeting and treating various cancers, including BC. Fucose-based CQDs offer biodegradability, biocompatibility, dispersibility in aqueous media, and antioxidant and anticancer properties [5]. They can efficiently deliver therapeutic payloads to BC cells while exhibiting intrinsic anticancer activity through the generation of reactive oxygen species (ROS). However, their binding affinity to various cell types, not exclusively cancer cells, raises concerns about binding to healthy cells as well. Additionally, the size heterogeneity of QDs affects their cellular uptake dynamics, with larger QDs facing challenges in penetrating cells, while smaller QDs demonstrate a higher likelihood of cellular entry, potentially causing damage. Nonetheless, fucose-based QDs show potential for targeted drug delivery in BC treatment with

---

the resolution of these challenges [6].

DC is a chemotherapy prodrug that exerts its anticancer effects through a multifaceted mode of action. Once administered, DC is metabolically activated in the liver, forming reactive metabolites that bind covalently to DNA molecules in cancer cells. This covalent binding leads to the cross-linking of DNA strands, disrupting the nucleic acid structure and inducing cell death across various phases of cellular division [7]. Although DC has shown efficacy in certain cancers like Hodgkin lymphoma and metastatic melanoma, its mechanisms and therapeutic potential in BC remain underexplored [8]. Challenges in its application to BC treatment arise from its poor aqueous solubility, susceptibility to photodegradation, and short biological half-life. These limitations can affect drug distribution, bioavailability, and treatment efficacy, and may lead to non-specific cytotoxic effects on healthy cells and adverse side effects [9,10].

In this study, we developed a strategy for targeted delivery of the chemotherapy drug DC to BC cells using CQDs. DC was loaded onto CQDs to improve its solubility and photostability and then encapsulated within Exo derived from BC cells (Ex-DC@CQDs) for therapeutic targeting. Exo can selectively target cancer cells through HSPG receptors and safeguard the integrity of DC and CQDs [11]. Exo expedite the conveyance of DC@CQDs to cancer cells by fusing with the cell membrane and facilitating the activation of DC specifically within cancer cells. Exo released by BC cells contain specific proteins (heparanase, syndecan-1, and glypican-1) that bind to HSPG receptors, accenting the involvement of the receptor in essential cellular processes. The interaction between Exo and HSPG receptors triggers an internalization process mediated by endocytosis [12]. This enables efficient delivery of exosomal cargo, including drugs, proteins, and nucleic acids, to the target cells, ensuring a targeted therapeutic approach. In addition, Exo isolated from BC cells are innately endowed with the capacity to express these vital cytochrome enzymes, which will facilitate activation of DC, negating the prerequisite for enzyme presence on the surface of cancer cells.

Therefore, it was hypothesized that cytochrome enzymes, particularly CYP1A1, CYP1A2, and CYP2E1, being integral parts of the Exo would facilitate direct activation of DC within the tumor microenvironment (TME) after HSPG-mediated spatial targeting of Ex-DC@CQDs into tumor cells, thereby engendering improved efficacy while minimizing untoward effects on normal cells [12]. Thus, Exo co-loaded with CQDs and DC can provide significant therapeutic effects against BC while avoiding the many risks associated with the free DC. Moreover, Exo possess an intrinsic ability to cross biological barriers, enabling them to encounter the phagocytosed drug lost during circulation. To achieve this, CQDs were initially prepared using the microwave method [13,14]. Subsequently, the developed CQD was loaded with DC, and the formulations were optimized to develop pharmaceutical specifications with higher loading and then characterized extensively both *in-vitro* and *in-vivo*. This amalgamation of DC@CQDs within BC cell-derived Exo is anticipated to emerge as a promising modality for the precise and targeted delivery of pharmaceutical agents to BC cells. Ex-DC@CQDs have the potential as an innovative therapeutic avenue for BC treatment.

2. Materials and methods

2.1. Materials

Dacarbazine, L-fucose, and PE-PEG were purchased from TCI (Toshima, Tokyo, Japan). Milli Q water, ethanol, PBS (pH 7.4) and propidium iodide (PI), protein ladder, ECL, nitrocellulose membrane and Anti-CD63, CD81, GAPDH and other antibodies were received from Cell Signaling Technology (CST) (USA). Gibco/Invitrogen (Life Technologies, USA) provided RPMI-1640, FBS, 0.25% trypsin-EDTA (1×), Antibiotics-antimycotic 100×, and the Exo isolation kit, whereas JC-1, DAPI, DCFDA, MTT were supplied from MP Biotech and the annexin-V tagged FITC/PI apoptosis kit was purchased from BD Biosciences.

HPLC-grade solvents such as MeOH and ACN were from Merck (India) while other necessary analytical-grade chemical reagents were sourced from various commercial suppliers. The details of making instruments and full names of chemicals and reagents have been provided in supporting information.

2.2. Methods

2.2.1. Preparation of L-Fucose Quantum Dots (CQDs)

The CQDs with nano-sized structures were prepared using a modified microwave technique. The method involved dissolving 0.0073 mol of L-fucose in 0.556 mol of an aqueous phase, followed by 0.01 mol of PE-PEG added into the solution [15,16]. The mixture was then subjected to microwave radiation at 800 Watt (W) for 5 min. At the final stage of the synthesis, the solution changes from colorless to yellowish brown, signifying the completion of the reaction. After microwave irradiation, the solution was gradually cooled to room temperature. The CQDs were extracted further by dissolving the carbonized brown-greyish product into deionized water, followed by ultrasonication (500 W) for 5 min [15–17]. This suspension was then centrifuged for 3 min at 1000 rpm to remove the big insoluble agglomerates or precipitate. The CQDs-containing supernatant was then filtered *via* a 0.22 μm membrane filter. The filtered solution was subsequently purified for 2 h in deionized water using dialysis (MWCO~3500 Da). The Fourier Transform Infrared Spectroscopy (FTIR) technique was employed for confirming the synthesis of CQDs in terms of functional group modification. Finally, the purified CQDs were placed in a amber colored glass container and preserved at 4 °C for further characterization and drug loading [15,18].

2.2.2. Loading of DC

To load the DC, a volume of 1.0 mL of DC (1.0 mg/mL) was added to 5.0 mL of CQDs PBS buffer solution (0.45 mg/mL) while being stirred for 6 h under cool and dark conditions [19]. The resulting suspension was repeatedly dialyzed against PBS buffer using a dialysis bag (MWCO ~1000 Da) to remove any unbound excess DC. The bath solution was replaced with fresh PBS buffer every 3 h until no absorption of DC at 326 nm was observed in the final PBS solution under UV-VIS Spectroscopy. The free drug content was determined by measuring the absorption at 326 nm of all bath solutions that were collected. Further, the FTIR technique was utilized to investigate the chemical interactions that may take place between DC and the other excipients. The traditional KBr disk/pellet approach was utilized to get FTIR spectra of both pure CQDs and DC@CQDs. The FTIR spectra were acquired with wave numbers ranging from 400 to 4000 cm-1.

2.2.3. Exosome isolation and encapsulation of developed DC@CQDs

Exo were extracted from the BC cell line (MDA-MB-468) after 2–3 passages, with 80–90% confluency using a previously reported method [20,21]. Initially, the collected cell supernatant was centrifuged at 2000 ×g for 10 min and the pellet was removed. The supernatant was then filtered through a 0.22 μm filter and again centrifuged at 12,000 ×g for 45 min [21]. The resulting supernatant was collected and filtered again, followed by ultracentrifugation at 120,000 ×g for 70 min. After the centrifugation, the supernatant was removed, and the pellet was resuspended in 10 mL of pre-cooled PBS. This step was repeated, and the Exo were finally obtained in 1 mL of pre-chilled PBS. The temperature during the entire procedure was kept at 4 °C. The resulting Exo were stored at −80 °C until further analysis [20]. The protein concentration of the suspension was calculated using a BCA kit. This modified method allowed for efficient and reliable isolation of Exo from BC cell lines, which is crucial for further downstream analysis. After isolation, the Exo were characterized using various techniques such as electron microscopy, NTA, and Western blotting to confirm the presence of Exo-specific markers such as CD63, and CD81.

Further, the Exo isolated from BC cells were coated onto DC@CQDs using the extrusion/sonication method. Briefly, the DC@CQDs were

mixed with Exo in PBS and subjected to sonication (20 kHz for 5 min, × 3 cycles) to create a homogeneous mixture. The mixture was then extruded through a filter, size 0.22 μm, to remove any aggregates or large particles. The extruded mixture was collected and washed with PBS to remove any unbound Exo. The temperature during the entire procedure was kept at 4 °C. The DC@CQDs-coated Exo (Ex-DC@CQDs) are characterized using various techniques such as DLS, NTA and confocal microscopy to confirm the presence of DC@CQDs and Exo. The formulation was stored at 4 °C in a dark and sterile container to prevent photo-degradation and contamination [22].

2.3. Characterization of developed formulation

2.3.1. Particle size, polydispersity index (PDI), zeta potential
The particle size, PDI, and potential of DC@CQDs and Ex-DC@CQDs were analyzed and compared using the DLS technique. Both samples were subjected to testing using the Malvern Zetasizer after being diluted a hundred-fold with triple-distilled water [23]. To ensure accuracy, each measurement was performed three times.

2.3.2. Surface morphology
TEM, HRTEM, SEM, and AFM techniques were used to analyze the morphology of the optimized formulation. For the TEM analysis, the formulation was dispersed onto a copper grid. After a 15-min settling period, a 4% *w/v* phosphotungstic acid solution was applied to the grid for negative staining. The samples were then air-dried at room temperature before imaging by TEM or HRTEM. Additionally, the SEM analysis was conducted using liquid formulation at a 3 kV acceleration voltage. Moreover, the developed formulation was also subjected to morphological evaluation using AFM performed with a non-contact mode. A cantilever (μ mash NSC15/AIBS) with dimensions of length 125 μm, width 35 μm, and tip radius of <10 nm was employed for this analysis [23,24].

2.3.3. Determination of entrapment and loading efficiency
The entrapment efficiency of DC in the final formulation (Ex-DC@CQDs) was evaluated using HPLC equipped with a reverse-phase C18 column, Endcapped (5 μm), and a PDA detector set to 293 nm. We have used a mixture containing 90 parts of MeOH and 10 parts of water with 0.1% formic acid as a mobile phase. Throughout the analysis, the autosampler compartment temperature was kept constant at 4 °C, and the injection volume was 20 μL [25]. The quantitative drug loading efficiency % LE and the entrapment efficiency %EE of DC in the formulation were calculated by using Eqs. (1) and (2), respectively.

$$LE(wt\%) = \frac{Amount\ of\ drug\ in\ formulation}{The\ total\ amount\ of\ lipid\ and\ drug} X100 \qquad (1)$$

$$EE(wt\%) = \frac{Amount\ of\ drug\ in\ formulation}{initially\ feeded\ drug} X100 \qquad (2)$$

2.4. In vitro release assay and storage stability

The *in vitro* release of Ex-DC@CQDs was carried out with the assistance of a dialysis bag system. Briefly, the Ex-DC@CQDs (dispersion equivalent to 1 mg of DC) was filled in a dialysis bag (with MWCO~12 kDa) and was added to 200 mL of pH 7.4 PBS that included 0.1% (*w/v*) of Tween 80. This was put on a magnetic stirrer, and the speed was set at 500 revolutions per min. The temperature was maintained at 37 °C [26]. Then a 1 mL sample was taken out at regular intervals and replaced with the same volume of the freshly prepared medium. The samples were examined by an HPLC technique. The analysis was carried out at three separate times. However, the storage stability was performed at a temperature of 4 °C for a period of one month. At certain intervals throughout the study, samples were collected and examined to determine the particle size and PDI.

2.5. Hemolysis assay

Fresh whole mouse blood was subjected to centrifugation at 1000 ×*g* for 5 min, and the supernatant was carefully removed. The resulting RBC pellet was washed and re-suspended in PBS. Subsequently, 50 mL of the RBC suspension (16% in PBS, *v/v*) was pooled with 1 mL of PBS, which served as the negative control, or various concentrations of Ex-DC@CQDs solutions dissolved in PBS [27]. Following incubation, the RBC suspensions were centrifuged again at 1000 ×*g* for 5 min, and the collected supernatants were retained [27]. The absorbance of the released hemoglobin (Hb) in the supernatants (200 μL) was subsequently measured at 540 nm using a microplate reader.

2.6. Cell culture

The BC cell lines 4 T1 and MDA-MB-231, as well as the MCF-7 cell line, were used in cell-associated studies. All the cell lines were grown in a culture medium consisting of RPMI-1640 supplemented with 10% *v/v* FBS, 100 I.U. penicillin, and 100 g/mL streptomycin. The incubation of the cells was carried out at a temperature of 37 °C in a humidified environment with 90% relative humidity and 5% CO₂. The flow cytometric analysis of all cellular studies was conducted using BD Biosciences, FACS Calibur, Germany [23].

2.7. Cytotoxicity study

For the *in vitro* cytotoxicity evaluation of free DC, CQDs, DC@CQDs, and Ex-DC@CQDs, the 4 T1, MCF7 and MDA-MB-231 cells were used and analyzed by the MTT assay. In brief, the cells were seeded in 96-well plates at a density of 3000–3500 cells/well and allowed to adhere overnight. The cells were then treated with all the formulations containing varying concentrations (ranging from 5 to 80 μM) of DC in RPMI media supplemented with 2% FBS, and incubated for 48 h. Following the incubation, the media was carefully removed, and 20 μL of MTT reagent (5 mg/mL) was added to each well. The plate was subsequently incubated at 37 °C in the dark for 3.5 h to allow the formation of formazan crystals. Afterward, the formazan crystals were dissolved by adding 100 μL of a DMSO/IPA mixture (1:1) to each well. The readout of the experiments was taken in a microplate reader at a wavelength of 570 nm, whereas the viability of the treated cells was normalized to that of the untreated cells present on the same plate [28].

2.8. Cell cycle arrest

MDA-MB-231 cells were grown in a 6-well plate to a density of 3 × 10⁵ cells/well and then treated for 48 h with free DC and different formulations at the concentrations mentioned above. Cells were washed with fresh PBS, trypsinized, and re-suspended in 500 μL cold 70% ethanol for 2 h at 4 °C. Following ethanol fixation, cells were centrifuged and re-suspended in 350 μL of fresh PBS. The cells were then treated with 50 μL (100 μg/mL) ribonuclease A (RNase A) and 100 μL (100 μg/mL) PI for 30 min. The flow cytometer was then used to examine the phase of cell arrest [29].

2.9. Mitochondrial membrane potential

The JC-1 dye was used to detect a depolarization in mitochondrial membrane potential (MMP), which is a crucial indicator of early apoptosis. JC-1 dye is a cationic, lipophilic dye that exhibits potential-dependent accumulation in mitochondria. Under normal conditions, JC-1 accumulates in the mitochondrial matrix, where it forms aggregates and emits red fluorescence. During early apoptosis or when the MMP decreases, JC-1 is unable to accumulate in the mitochondria effectively. Instead, it remains in the cytoplasm as monomers, resulting in green fluorescence. In brief, MDA-MB-231 cells were seeded in six-well plates (4 × 10⁵ cells/ well) and incubated for 48 h in media

containing free DC, CQDs, DC@CQDs, and Ex-DC@CQDs at 37 °C. After incubation, the cells were washed, trypsinized, and re-suspended in 500 μL of PBS added with JC-1 dye (3 μg/mL) [23]. Thereafter, the cell suspension was analyzed with a flow cytometer. Untreated cells were taken as the control.

2.10. Apoptosis

For the detection of apoptosis, an annexin V and PI Kit were used as directed by the manufacturer's instructions. Briefly, MDA-MB-231 cells were seeded at the density of 1×10^5 cells/well in 6 well plates and treated with free DC, CQDs, DC@CQDs, and Ex-DC@CQDs, and untreated for 48 h. Following the incubations, cells were suspended in 500 μL PBS, centrifuged at 3000 rpm for 5 min, and then re-suspended in 500 μL PBS. Annexin V FITC and PI 5 μL each were added to this and incubated for 15 min at room temperature in a dark area. Flow cytometry was conducted using a FACS, equipped with a single 488 nm argon laser (Becton Dickinson, Mountain View, CA) [30,31]. Debris and clumps were gated out using forward and orthogonal light scatter.

2.11. Cellular uptake and cell imaging studies

2.11.1. Flow cytometry

To quantitatively evaluate the uptake of the developed formulation in MBA-MB 231 and 4 T1 cells, flow cytometry analysis was performed using a BD calibur flow cytometer. The cells were seeded at a density of 3×10^5 cells/well and incubated overnight at 37 °C in a 5% CO$_2$ incubator. Subsequently, the cells were treated with Ex-DC@CQDs and DC@CQDs formulations at different time points. The fluorescence associated with cell uptake was then measured at each time interval.

2.11.2. Confocal microscopy

The MDA-MB-231 cells and 4 T1 cells were grown overnight in RPMI media supplemented with 10% FBS and 1% penicillin/streptomycin in a cell culture disk. After the cells had grown well, following the treatment, incubated for various time points at 37 °C in a 5% CO$_2$ incubator. Subsequently, the cells were washed twice with PBS pH 7.4, and excessive non-internalized formulation was removed. Imaging was accomplished in a confocal microscope [32].

2.12. Receptor blocking

To investigate the increased cellular uptake of the Ex-DC@CQDs formulation *via* HSPG receptors, MDA-MB-231 and 4 T1 cells were subjected to a receptor-blocking study. The cells were initially seeded in 6 well plates and allowed to adhere for 24 h. Subsequently, the adhered cells were rinsed with PBS (pH 7.4) and incubated with serum-free media with or without anti-integrin of 1 μM for 2 h at 37 °C in a CO$_2$ incubator. Following the incubation, the cells were washed with PBS and treated with fresh medium containing Nile red-tagged Ex-DC@CQDs and DC@CQDs. The cells were then incubated for 6 h and afterward, the cells were harvested by trypsinization, subjected to two washes to remove any unbound particles and dye, and re-suspended in 450 μL of PBS for subsequent flow cytometry analysis.

2.13. Reactive oxygen species production

To evaluate the generation of ROS in cells treated with CQD and DC encapsulated formulations, a DCFDA assay was performed. The cells were treated with each formulation at an equivalent concentration of 20 μM for 48 h at 37 °C in the incubator. Following the treatment, the cells were incubated with a dye solution of DCFDA (10 μM) for 0.5 h at room temperature. Subsequently, the cells were washed, harvested, and suspended in PBS. The resulting ROS generation was determined by measuring the fluorescence intensity of 2, 7-dichlorofluorescein (DCF) using a flow cytometer [33]. All experiments were conducted in triplicate to ensure accuracy and reproducibility.

2.14. Western blotting

The protein samples were acquired by subjecting the harvested cells to incubation with RIPA buffer in an ice bucket for a duration of 20–30 min. Subsequently, the samples were centrifuged at 4 °C and 12,000 rpm for 20 min. Protein quantification and separation were achieved using a BCA protein assay kit and 10–15% SDS-PAGE. The separated proteins were then transferred to a PVDF membrane and blocked with a 5% BSA solution at room temperature for 1 h. The membrane was washed three times with TBST. For protein detection, the membrane was incubated overnight at 4 °C with primary antibodies specific to the target proteins of interest. Subsequently, a secondary antibody was applied and allowed to incubate for 2 h, followed by further washing steps. The immune-reactive proteins were visualized using ECL reagents in a Chemi Doc system. The GAPDH was utilized as a loading control [34].

2.15. 4T1-tumor xenograft model and tumor regression study

The xenograft BC model was developed in Balb/c female mice (3–4 weeks young; weight 16–20 g). Initially, the 4T1 mammary cancer cell lines with a cell count of 5×10^6 were administered in the mammary fat pad near the left lower abdominal quadrant with an equal proportional volume of Matrigel. When the tumor reached 100–110 mm^3, the animals were randomly divided into five groups ($n = 5$) and administered saline control, free DC, CQDs, DC@CQDs, and Ex-DC@CQDs intravenously (IV) *via* tail veins on days 0, 4, 7, 10, 13, 16, and 19. Tumor volumes were calculated using the formula V = $\pi/6 \times$(L) x (W)^2, where L is the largest tumor diameter in mm and W is the smallest tumor diameter in mm. Other parameters observed in the animals included survival, body weight, and behavior [27]. Following the completion of the study, the animals were terminated, and histological samples were taken from vital organs and tumor. All animal experiments were carried out in accordance with the guidelines for the care and use of laboratory animals, as well as with the approval of the CSIR-CDRI Institutional Animal Ethical Committee (IAEC/2021/80/Renew-1).

2.16. Pharmacokinetic and tissue drug distribution

To examine the *in vivo* pharmacokinetics and tissue distribution, the developed drug-loaded formulations were administered through the IV route at dosages equivalent to 10 mg/kg in a BC-induced mouse model. The mice were segregated into three groups: Group-I for free DC, Group-II for DC@CQDs, and Group-III for Ex-DC@CQDs formulations. After the single IV dose in these animal groups, 200 μL of blood was drawn from the retro-orbital plexus at predefined time intervals. Prior to sacrificing the animals for organ isolation, only two blood samples were obtained from each animal. Subsequently, all the collected organs (liver, spleen, heart, kidney, and tumors) were individually homogenized in PBS to create a tissue homogenate for drug analysis, and this tissue homogenate was extracted using the same method as in serum [35].

To determine the concentrations of the DC and its active metabolite [5-amino-1H-imidazole-4-carboxamide (AIC)], a validated LCMS method was employed. For analysis, the mobile phase composed of methanol (A) and milli-Q water containing 0.1% FA (B) was chosen. The NOVA pack C18 column isocratic flow system in a 55:45 ratio (A:B) was used. A flow rate of 0.5 mL/min and injection volume of 10 μL/min was maintained for 10 min. The serum concentration-time profiles were calculated using GastroPlus software, employing non-compartmental analysis.

2.17. Optical in vivo imaging of developed formulation

To assess the *in vivo* biodistribution of Ex-DC@CQDs, real-time NIRF imaging was employed. Briefly, the developed formulation was labeled
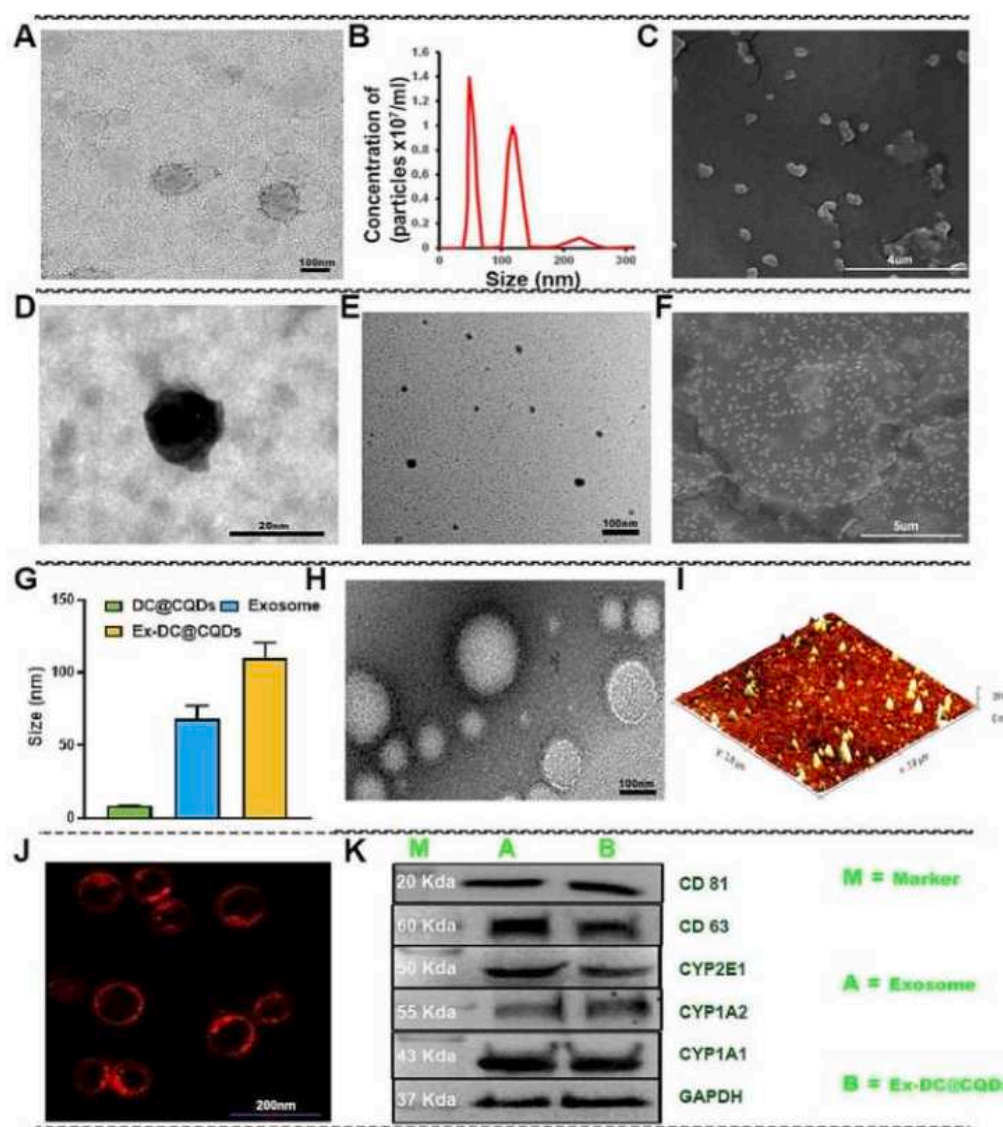
Fig. 1. Morphological and surface characterization. (A) Characterization of MD-MB-468 isolated Exo by TEM image. (B) Size characteristic and intensity of Exo through NTA. (C) SEM image of Exo. (D) TEM image of synthesized DC@CQDs. (E) HR-TEM image of DC@CQDs. (F) SEM image of DC@CQDs. (G) The relative particle size of developed formulation. (H) TEM image of Ex-DC@CQDs. (I) 3D AFM image of DC@CQDs. (J) Confocal based characteristic presence of HSPG protein following staining with syndican1 antibody (Catalog # MA5–32600) on Exo. (K) Characteristic presence of marker of Exo exploration by Western blot analysis. All the data were present as $n = 3$.

using Evans blue dye, and vortexed for 10 min. Subsequently, the formulations underwent centrifugation, and the resulting formulation pellets were reconstituted in a PBS solution to get rid of the free dye. Following IV injection of Evans blue-labeled DC@CQDs and Ex-DC@CQDs, tumor-bearing mice were longitudinally imaged using an IVIS Spectrum system. The mice having tumors of between 200 and 300 mm^3 were used for the experiment. To analyze the tissue distribution of the developed formulation, the tumors and key organs were surgically removed for *ex vivo* NIRF imaging over 24 h after the injection. Afterward, each organ was carefully cleaned with saline and scanned. The fluorescence intensity at each specific location relative to the organ surface was calculated using radiant efficiency [23].

2.18. Statistics

Statistical analysis was performed on the obtained data, and the statistical values were presented as mean ± standard deviation (SD) based on a minimum of three independent experiments. The various groups were subjected to a one-way analysis of variance (ANOVA) and probability values <0.05 or < 0.001 were considered as statistically significant. The data were analyzed by Graph Pad Prism version 9.4. 1 (a trial version).

3. Results and discussion

3.1. In vitro characterization of Ex-DC@CQDs

Fucose-in-water-and-PE-PEG-based CQDs were developed and optimized by slightly modifying the reported method [36,37]. The optimized CQDs were then selected and further incubated with DC to successfully load the drug, resulting in the development of DC@CQDs [38]. Afterward, the DC@CQDs were effectively loaded into isolated and purified Exo using a previously reported method, leading to the formation of Ex-DC@CQDs [39,40]. The DC@CQDs exhibited a size range of 2–10 nm (Average particle size, APS, 8.25 ± 0.23 nm; PDI 0.21 ± 0.05), which was suitable for their loading into extracellular vesicles

Table 1
Particle characteristics and DLE of the targeted and non-targeted formulation.

Sample	Size (nm)	PDI	Zeta potential (mV)	DLE (%w/w)
DC@CQDs	8.25 ± 0.23	0.21 ± 0.05	−26.7 ± 7.73	10.12 ± 1.5
Ex-DC@CQDs	110.70 ± 10.0	0.18 ± 0.09	−34.6 ± 6.41	12.08 ± 1.1

[39,40]. However, the size of the Exo was slightly higher (50–300 nm, Fig. 1A, C); consequently, the APS for the final formulation (Ex-DC@CQDs) (APS, 110.70 ± 10.0 nm; PDI 0.18 ± 0.09) increased (Fig. 1G). Nanocarriers within the size range of 50–300 nm are known to have improved localization at the tumor site, benefiting from the enhanced permeability and retention (EPR) effect [41]. Moreover, the surface potentials of DC@CQDs and Ex-DC@CQDs were measured to be −26.7 ± 7.73 mV and − 34.6 ± 6.41 mV, respectively (Fig. S1, D—F), indicating promising stability of the dispersion system and suitability for IV administration [42]. As stated previously, a decrease in the zeta potential of the final formulation indicates increased colloidal stability of the formulation [42].

The surface morphology and spatial integrity of the developed formulations were examined using SEM, TEM, and AFM. These imaging techniques confirmed that DC@CQDs exhibited a spherical shape within a narrow size range of <20 nm [TEM: 4–8 nm (Fig. 1D), SEM: 15–20 nm (Fig. 1F), AFM: 10–15 nm]. In contrast, Ex-DC@CQDs showed a relatively larger size [TEM: 100–200 nm (Fig. 1H)] compared to the unloaded exosomal dispersion (50–120 nm). Three-dimensional surface topographical observations conducted using AFM further supported these findings (Figs. 1I and S1, A-B).

The HRTEM image in Fig. 1E shows clear lattice fringes with an interplanar spacing of 0.28 nm, which is consistent with other reported CQDs, indicating a crystal structure. Furthermore, the crystallinity of the developed formulation was also determined by SAED pattern (Fig. S1C). The loading of DC@CQDs into Exo resulted in an increase in size, which is expected. Moreover, the APS of Ex-DC@CQDs falls within an acceptable range for delivery [41]. The entrapment and loading efficiencies of the targeted formulation (Ex-DC@CQDs) were observed to be 86.45 ± 7.9% and 12.08 ± 2.1%, respectively. In contrast, the non-targeted formulation (DC@CQDs) showed an estimated drug loading of 10.12 ± 1.5% (Table 1).

3.2. Fourier transform infrared spectroscopy

FTIR was also done to ascertain the development of DC@CQDs. The stretching frequency (C—H) of DC was detected in the range of 2911 cm^{-1} in the FTIR spectrum for DC@CQDs [43]. The vibrational spectra of -NH amine and amide were recorded at 3418 cm^{-1} and 1641 cm^{-1}, respectively, as well as C—N and stretching at 1398 cm^{-1} [43]. The presence of Fucose QDs is displayed by the -OH aromatic and aliphatic vibrational frequencies at 3413 cm-1 and 941 cm^{-1}, respectively, with absorption bands at 2907 cm^{-1} which is attributable to the stretching
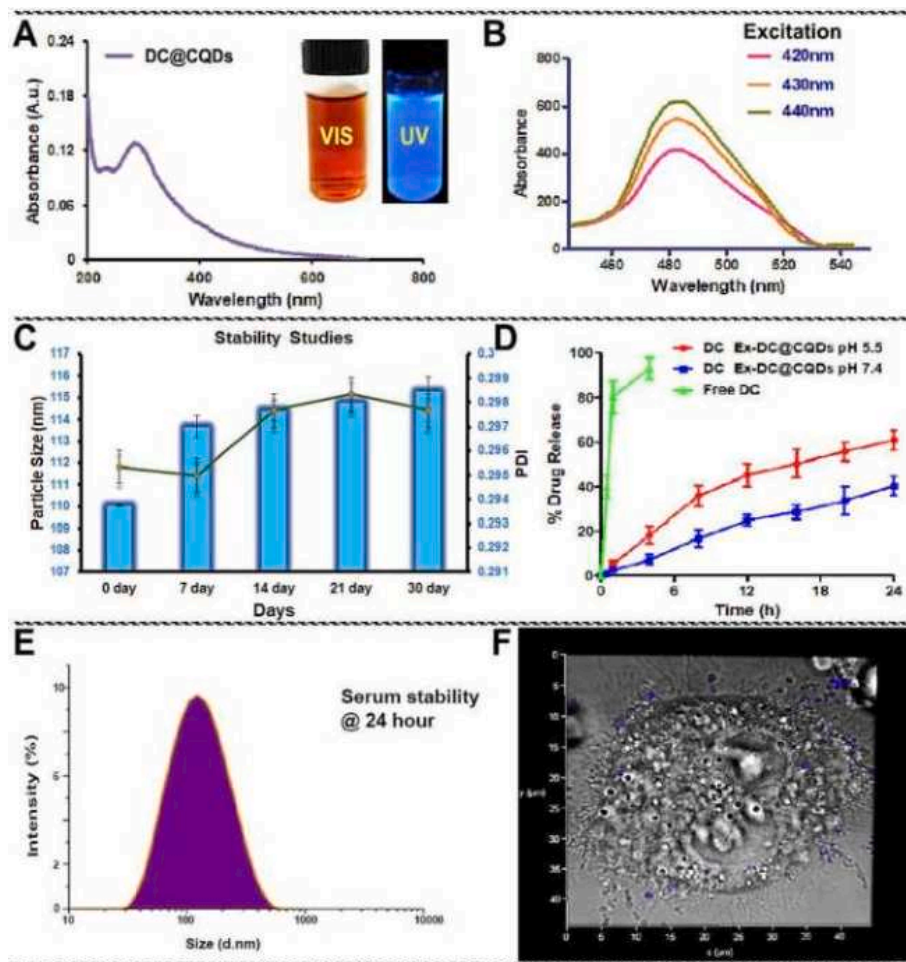

Fig. 2. (A, B) Fluorescent photograph and spectrum of DC@CQDs upon UV illumination (366 nm). (C) The physical stability of the Ex-DC@CQDs. (D) % Drug release from Ex-DC@CQDs at pH 7.4 and 5.5. (E) Serum stability study of Ex-DC@CQDs. (F) 3D confocal microscopic imaging of particle internalization (DC@CQDs) in the MDA-MB-231 cell line. All the data were recorded ($n = 3$).
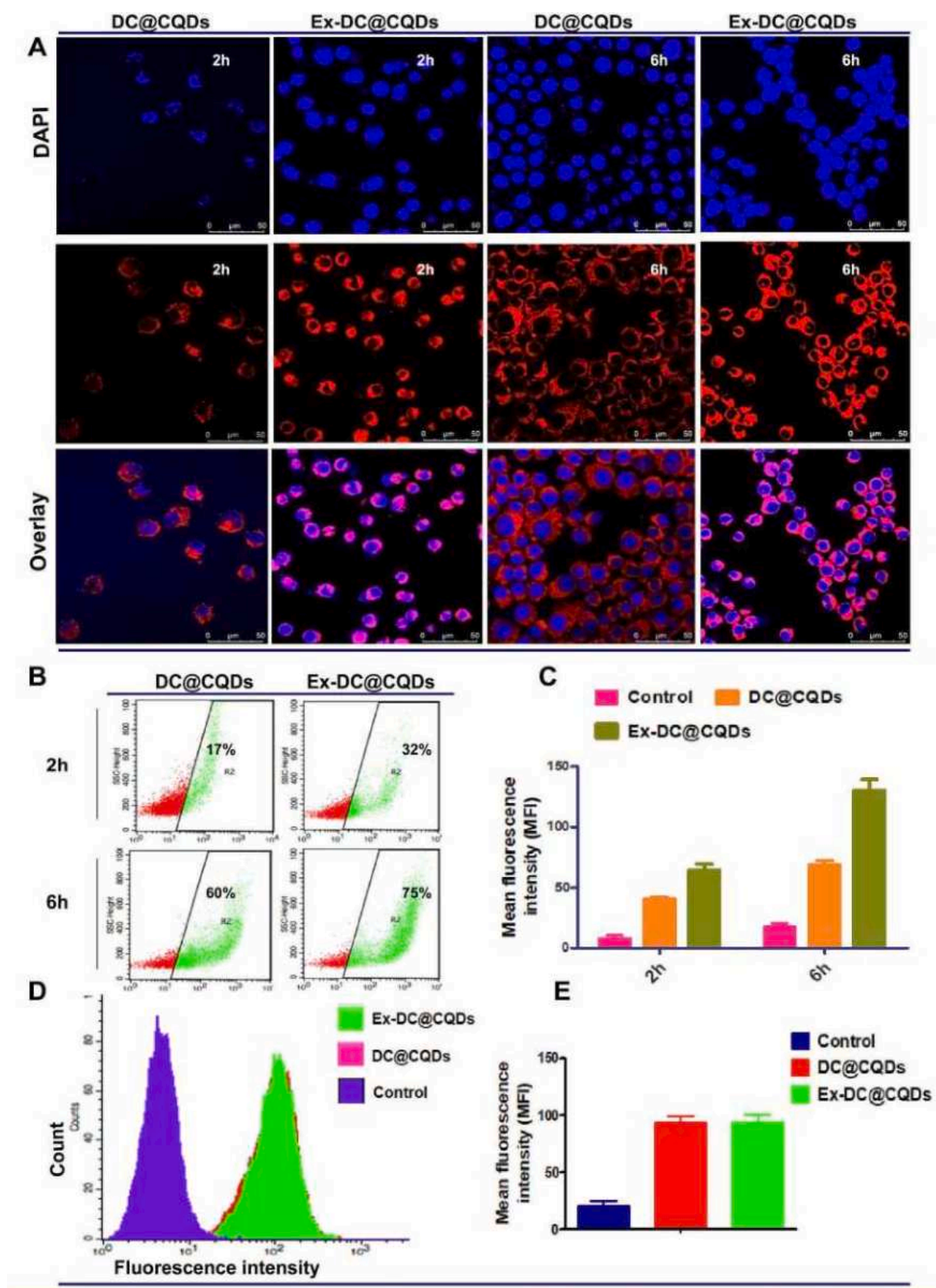
Fig. 3. (A-C) The qualitative and quantitative assessments of Nile red-tagged Exo encapsulated formulation (Nile Red- DC@CQDs and Ex-DC@CQDs) after 2 and 6 h treatment of MDA-MB-231 cells using confocal microscopy. (B) Flow cytometry-based quantitative estimation of the cellular uptake in MDA-MB-231 cells following incubation for 2 and 6 h. (D-E) Receptor blocking study in MDA-MB-231 cells. All the experiments were achieved in triplicate ($n = 3$).

frequency (-CH) in Fucose [44]. Further, PEG displayed vibrational spectra for (C-O-C) at 1094, 1248 and 1297 cm^{-1} and for (-CH) and (C=C) at 2902 and 1646 cm^{-1}, respectively. The IR frequency of CQDs and DC@QDs is depicted in Fig. S2A.

3.3. Nano tracking analysis and Western blotting

The hydrodynamic particle sizing through NTA in each milliliter formulation dispersion (Ex-DC@CQDs) ensured an overall Exo diameter < 100 nm; however, the number of Exo between 100 and 300 nm was low (Fig. 1B). Further, it is essential that Exo retain all their structural and functional characteristics after being extracted from the parent cell to carry out their function as tumor cell targets. The Exo formulation (Ex-DC@CQDs) exhibited expressions of their specific markers, including CD81, CD63, CYP2E1, CYP1A1, and CYP1A2, in Western blotting (Fig. 1K) [45]. The significant levels of expression of these proteins were observed in the isolated Exo and in the Ex-DC@CQDs. Also, the protein expression of CYP1A1, CYP1A2 and CYP2E1 in Ex-DC@CQDs ensured the site-specific conversion of DC into an active form under favorable TME, suggesting that Exo may serve as delivery vehicles with structural and functional integrity [21,46].

3.4. The optical properties of carbon quantum dots

The photoluminescence (PL) properties of quantum dots are attributed to their component and respective functional groups that play a vital role in overall features [44]. When exposed to light, aromatic compounds undergo distinct excitation and relaxation processes, resulting in the emission of fluorescence. The presence of aromatic hydroxyl groups on the surface of quantum dots establishes an abundance of π-electron systems, serving as fluorescent centers. These centers proficiently absorb excitation energy and subsequently release light, yielding fluorescence. The UV–vis absorption spectrum of quantum dots exhibits a pronounced capacity for light absorption at a specific wavelength of approximately 326 nm (Fig. 2A). This absorption phenomenon can be attributed to the presence of distinctive chemical bonds within the quantum dots, namely the aromatic C=C bond and the sp2 system housing C=O and C=N bonds. When these bonds capture light, a π-π* or n-π* transition occurs, triggering vibrations and the subsequent emission of light at an altered wavelength [44]. Markedly, the emission of bright blue fluorescence emerges when quantum dots are excited with UV light at 366 nm, owing to these reported transitions. The optimal excitation wavelength for fluorescence detection in the context of quantum dots was determined to be 488 nm (Fig. 2B). Moreover, the fluorescence quantum yield of the generated quantum dots has been reported to be 0.54, featuring their notable luminous efficiency. To investigate fluorescence characteristics further, the fluorescence lifetime was accurately calculated utilizing a transient fluorescence spectrometer, which offers insights into the duration that quantum dots remain in their excited states before reverting to their ground states. Furthermore, the decay trace of the PL intensity of the quantum dots was precisely ascertained through the utilization of multi-exponential functions (t) and a non-linear least squares methodology [44].

3.5. Drug release, storage stability, and hemocompatibility

The release of DC from Ex-DC@CQDs is depicted in Fig. 2 at pH 5.5 and 7.4. Ex-DC@CQDs demonstrated the release of approximately 60% of the DC in 24 h at pH 5.5; however, when the pH was 7.4, only 40% of the drug was released under the same conditions. The release of DC from Ex-DC@CQDs was considerably faster in an acidic environment, corresponding to TME, and significantly slower at a pH of 7.4, corresponding to the remaining and more abundant physiological pH in the body. The acidic environment could alter the structure of the formulation, composed of carbohydrates and phospholipid causing the release of DC from the structure and leading to an accelerated and higher drug release

from Ex-DC@CQDs compared to an alkaline or neutral environment [47,48]. The cumulative DC release from Ex-DC@CQDs was 1.5 times-higher at pH 5.5 than at pH 7.4. Further, the stability of Ex-DC@CQDs was monitored in PBS at 4 °C for one month (pH 7.4). The formulation did not show any signs of clumping, and no change in either its size or its PDI was evident during the storage (Fig. 2C). In addition, to ensure the biological stability of the Ex-DC@CQDs, *i.e.*, serum, the formulation was cultured in 10% FBS, generally used in the cell culture, and the size of the Ex-DC@CQDs was measured. Incubation in serum for 12 or 24 h did not result in a significant reduction or increase in particle size. The results showed that the physical stability of Ex-DC@CQDs is unaffected by the presence of serum proteins (Fig. 2E). Evaluation of *in vitro* hemocompatibility of formulations provides an insight into *in vivo* compatibility of the nanocarrier. The hemolytic study was carried out using formulations with different concentrations ranging from 100 to 500 μM. The formulation (Ex-DC@CQDs) and free drugs with the highest concentration showed a range of 3–5% hemolysis (Fig. S2B), in comparison to the positive control, while all other formulations showed below this value [49]. This suggests the safe use and hemocompatibility of Ex-DC@CQDs formulation in *in-vivo* experimentation.

3.6. Exosome facilitated cellular uptake

The cellular uptake of the developed formulation (DC@CQDs and Ex-DC@CQDs) through the HSPG receptor was examined using CLSM and flow cytometry techniques. To investigate this, MDA-MB-231 (Fig. 3A) and 4T1 (Fig. S3A) cells were treated with Nile red-tagged DC@CQDs and Ex-DC@CQDs for 2 and 6 h, respectively, while all treatment groups exhibited an increase in fluorescence intensity over time, the Exo-encapsulated (Ex-DC@CQDs) showed the strongest signal, followed by the non-targeted group (DC@CQDs), and the lowest fluorescence intensity was observed in the Nile red-blank treated group. Furthermore, the fluorescence intensity of Ex-DC@CQDs increased over time in both MDA-MB-231 and 4T1 cell lines (Fig. 3B─C); the internalization capacity was also evaluated in a concentration-dependent manner following the treatment with 5, 10 and 15 μM equivalent Ex-DC@CQDs formulation in the MDA-MB-231 cell line (Fig. S4, C, D), indicating the overall ability of the Exo-encapsulated formulation to enhance cellular trafficking across cell membranes. The CSLM results revealed that the targeted formulation's fluorescence intensity was initially found in the cytoplasm and nucleus regions of the cells within 2 h, and subsequently diffused into the nucleus over the next 6 h. Additionally, the enhanced accumulation of Ex-DC@CQDs in the cytoplasm was observed through differential fluorescence intensity, which can be attributed to the HSPG protein on the formulation's surface, acting as a targeting motif that complements the HSPG surface receptor (Fig. 1J) [50]. Further, it was observed that Ex-DC@CQDs exhibited a higher fluorescence intensity in cancer cells after 6 h of treatment compared to that at the initial time, providing further evidence of the remarkable uptake capacity of Ex-DC@CQDs. As an additional measure to ensure formulation internalization into cancer cells, the auto-fluorescent property of CQDs loaded within Ex-DC@CQDs was investigated. MDA-MB-231 cells were exposed to DC@CQDs (without any cellular fluorescent dye) for 6 h, and the results demonstrated clear internalization of Ex-DC@CQDs, showing a blue-colored spot corresponding to the auto-fluorescent emission of CQDs on the outer surface of the cell. However, after internalization, the spot appeared dull, greyish, and silvery due to the cell membrane covering, confirming the effective internalization of DC@CQDs (Fig. 2F). Moreover, it is known that cancer cells possess HSPG-specific receptors, and Exo with HSPG protein preferentially interacts with these receptors, triggering receptor-mediated endocytosis in these cells [50]. To confirm that Ex-DC@CQDs undergo receptor-mediated endocytosis, a receptor-blocking study was conducted. Highly metastatic cell lines, such as MDA-MB-231 and 4T1, which express a higher level of HSPG receptors on their cell surface, were used for this study. The cells were pre-treated with 1 μM integrin antibody to saturate the receptors [51],
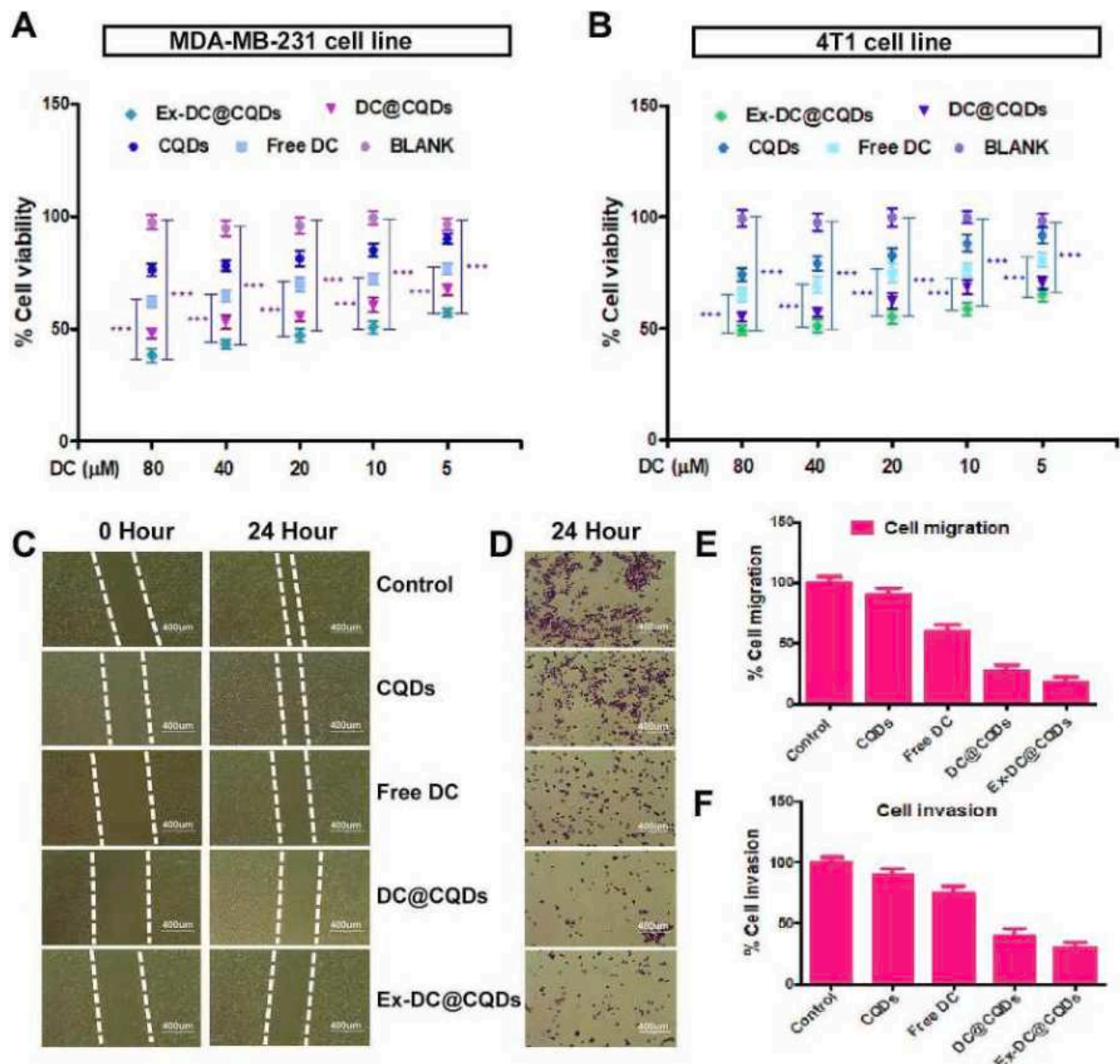
Fig. 4. (A) MTT assay for cell viability in MDA-MB-231 cells, followed by 48 h of treatment with different sample groups, and (B) Cell viability in 4 T1 cells. (C and E) Cell migration at 0 and 24 h. (D and F) Cell invasion at 24 h. All the experiments were achieved in triplicate ($n = 3$).

and then both the non-targeted (DC@CQDs) and Exo-encapsulated (Ex-DC@CQDs) formulations were treated to demonstrate and validate the role of HSPG receptors in endocytosis. Subsequently (Fig. 3D-E), it was observed that after 6 h of treatment, the average fluorescence intensities of both formulations were almost identical, indicating that the interaction between HSPG and the HSPG receptor played a crucial role in enhancing cellular uptake inside the cells [12,52].

3.7. Cell viability

The MTT assay was performed to assess cell viability in MDA-MB-231, MCF7 and 4 T1 cell lines following treatment to free DC, CQDs, DC@CQDs, and Ex-DC@CQDs. The cell viability was monitored for a period of 48 h, during which a dose-dependent decline in viability was observed (Figs. 4, A-B and S4E).

Furthermore, the GraphPad Prism software was used to determine the IC50 values for different formulations. Ex-DC@CQDs had lower IC50 values compared to DC@CQDs in three cell lines: MDA-MB-231 (Ex-DC@CQDs: 20 μM, DC@CQDs: 40.5 μM), 4T1 (Ex-DC@CQDs: 34 μM,

DC@CQDs: 52 μM), and MCF-7 (Ex-DC@CQDs: 47.7 μM, DC@CQDs: 82.42 μM). The results revealed that Ex-DC@CQDs exhibited a 2.02-fold lower IC50 value for MDA-MB-231 cells, a 1.52-fold lower IC50 value for 4T1 cells, and a 1.72-fold lower IC50 value for MCF7 cells compared to the DC@CQDs-treated formulation.

Notably, Ex-DC@CQDs exhibited significantly higher toxicity against cancer cells compared to free DC and other treatment groups. This enhanced toxicity can be attributed to several factors, including improved cell uptake, efficient endosomal escape facilitated by the encapsulation with Exo, and enhanced intracellular release triggered by the pH conditions within the cells. The free DC exhibited lower cytotoxicity than Ex-DC@CQDs, likely to be removed from cells through rapid efflux mediated by the p-glycoprotein pump [53].

3.8. Effect of different formulations on cell cycle arrest, apoptosis, and alteration of MMP

Cell cycle arrest, apoptosis, and MMP were examined using flow cytometry to compare the effects of DC in its free form and as a
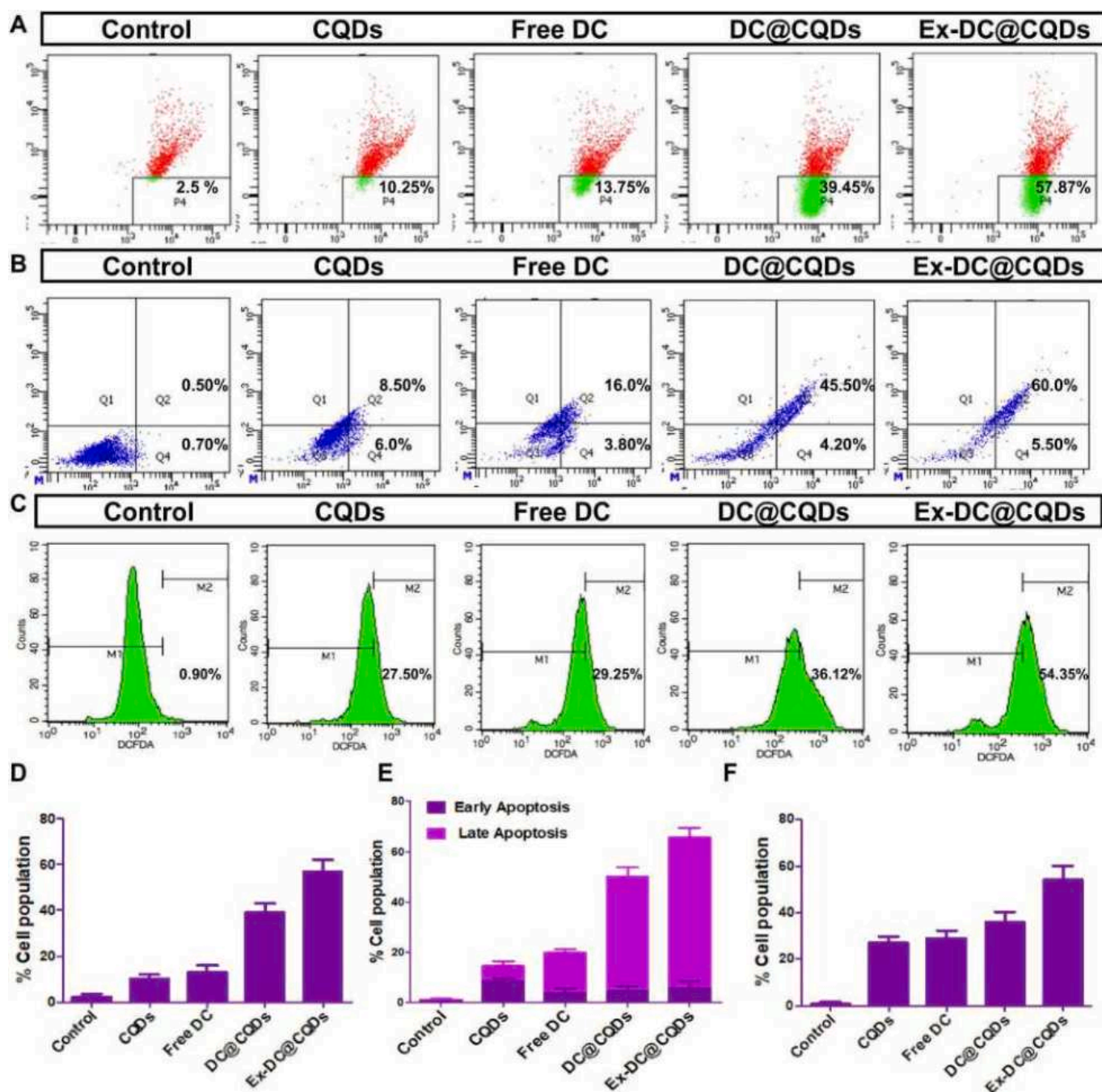
Fig. 5. Flow cytometry data for MMP, apoptosis, and ROS in the MDA-MB-231 cell line. (A and D) Representative % depolarization of MMP after 48 h of treatment. (B and E) Results in early and late apoptosis in MDA-MB-231 cells following 48 h of incubation. (C and F) ROS generation after 48 h of treatment. These results were obtained in triplicate ($n = 3$) mean SD.

formulation within Exo. DC is an anticancer drug that has been extensively studied for its ability to halt cancer cells in the G1 or S phase [54]. Based on our observations, cells treated with free DC displayed a notable arrest in the G1 and S phases. In contrast, Ex-DC@CQDs induced cell cycle arrest in the G1, S, and G2-M phases, potentially attributed to the presence of CQDs that influenced the G2-M phase arrest [54]. However, the precise mechanism by which CQDs trigger G2-M phase arrest remains unexplored. It is plausible that the involvement of CQDs in apoptosis and the subsequent production of ROS following DNA damage might contribute to the G2-M phase cell cycle arrest [5,56,57].

Furthermore, when comparing the effects of free DC, CQDs, DC@CQDs, and Ex-DC@CQDs, it was observed that Ex-DC@CQDs caused a lesser arrest in the G1 phase and relatively higher inhibition

in the S and G2-M phases (Fig. S4, A-B).

Further, the MDA-MB-231 cells treated with Ex-DC@CQDs exhibited a higher degree of apoptosis in the cancer cell population compared to non-targeted DC@CQDs and free drug, which was significantly corroborated with the outcomes from cell cycle arrest. Treatment with free DC and CQDs showed almost $19.8 \pm 2.3\%$ and $14.5 \pm 1.8\%$ apoptosis, respectively (Fig. 5B and E). However, a total of $65.5\% \pm 7.5\%$ apoptotic population comprising early and late apoptosis was seen following treatment with Ex-DC@CQDs. In addition to this, it was noticed that the DC@CQDs had an added effect on the enhancement of DC sensitivity. Also, the depolarization of the mitochondrial membrane was observed in $13 \pm 2.5\%$ and $10 \pm 2.1\%$ of the cell population by free DC and CQDs, respectively. The non-targeted therapy merely increased
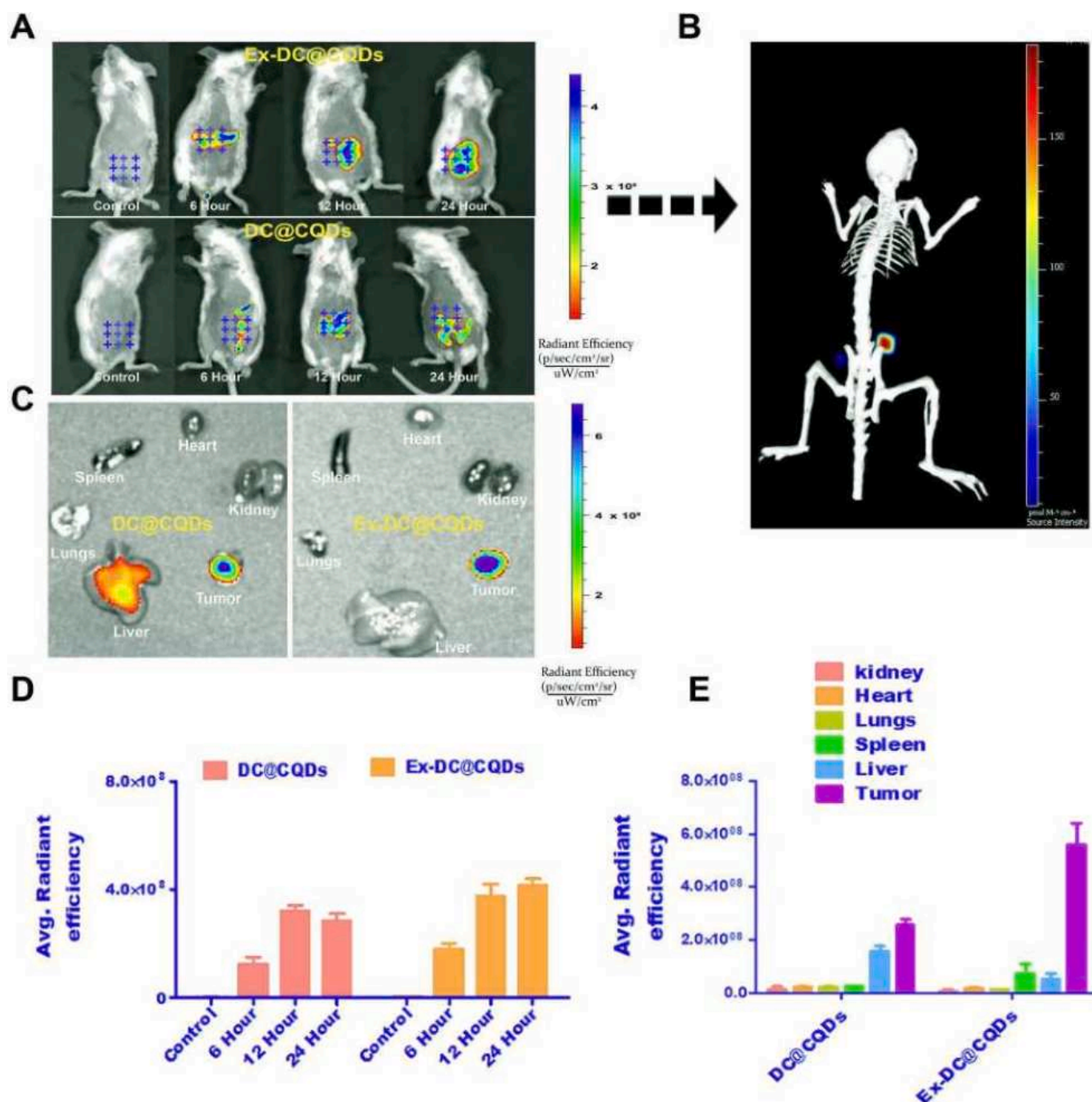
Fig. 6. Visualization of *In vivo* imaging and tumor-targeting study after IV administration of Evans blue-labeled developed formulation. (A) Whole-body image comparing targeted and non-targeted groups. (B) Three-dimensional *In vivo* imaging model. (C) *Ex vivo* imaging of vital organs from the same experimental setup. (D) Quantitative assessment of the fluorescence intensity specific to tumors in groups of animals treated with Ex-DC@CQDs and DC@CQDs formulations. (E) *Ex vivo* quantitative assessment of fluorescence signals in vital organs. All data are expressed as mean ± standard deviation (*n* = 3). (For interpretation of the references to colour in this figure legend, the reader is referred to the web version of this article.)

depolarization by 39 ± 3.5%; however, Ex-DC@CQDs showed a cumulative 57 ± 7.1% increase in depolarization relative to the other treatment groups (Fig. 5A and D). Altogether, these outcomes indicate that CQDs may significantly enhance the sensitivity of DC as a free drug or in Exo formulation, apparently *via* cell cycle arrest and synergistic mitochondrial depolarization leading to higher apoptosis.

3.9. ROS studies

The generation of intracellular ROS plays a crucial role in inducing DNA damage and cell membrane destruction, ultimately leading to apoptosis in cancer cells [58]. The effects of different treatments such as free DC, CQDs (27.50 ± 1.44%), DC@CQDs (36.12 ± 4.34%), and Ex-DC@CQDs (54.35 ± 5.21%) on intracellular ROS production were observed. MDA-MB-231 cells were subjected to analysis using DCF fluorescence. The intracellular uptake of DCFDA and subsequent interaction with cellular esterase resulted in the formation of the DCF fluorescence, which enabled the detection of ROS by measuring the fluorescence intensity. An increased ROS production caused by the CQDs was reflected in significantly higher mean fluorescence intensity
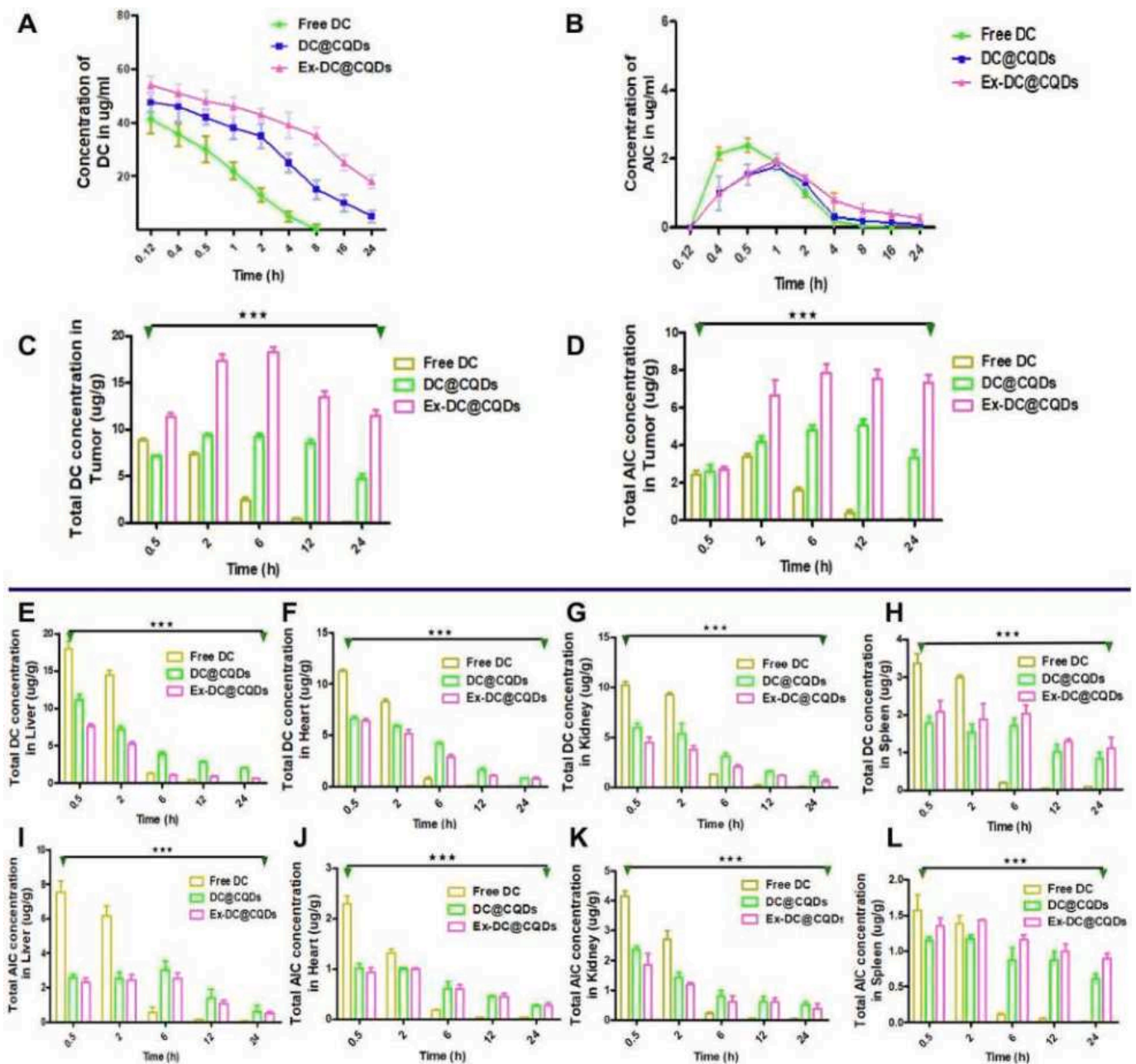
Fig. 7. Drug distribution studies in BC mice model after single IV administration of free DC and various formulations. (A-B) Quantitative estimation of DC and metabolite AIC in the serum following IV administration of 10 mg/kg equivalent DC in Free DC, DC@CQDs, and Ex-DC@CQDs treated groups. (C, *E-H*) Distribution of DC after IV administration of free DC, DC@CQDs, and Ex-DC@CQDs in the tumor, liver, heart, kidney and spleen respectively. (D, I-L) Simultaneously a quantitative analysis was conducted to determine the conversion of metabolite AIC following intravenous administration of Free DC, DC@CQDs, and Ex-DC@CQDs in the tumor, liver, heart, kidney, and spleen respectively. All data are expressed as mean ± SD ($n = 6$).

in cells treated with Ex-DC@CQDs, exerting more apoptosis compared to those treated with DC@CQDs or free DC alone (Fig. 5C and F) [59].

3.10. Cell migration and invasion assay

The effect of Ex-DC@CQDs, which were coated with Exo, on cell invasion and migration was investigated using a wound healing or scratch assay in the highly metastatic HSPG receptor expressing MDA-MB-231 cell line. The untreated control groups exhibited a higher degree of cell migration, with nearly complete coverage of the wound area within 24 h of initiating the wound (Fig. 4, C—F). Conversely, the treatment groups showed a reduction in cell migration and a simultaneous decrease in the number of cells within the wound gap, with the Ex-

DC@CQDs treated group displaying the lowest cell count within the gap.

3.11. In vivo imaging study

To investigate the bio-distribution of Ex-DC@CQDs at the tumor site, Balb/c tumor-bearing mice induced with 4 T1 cells were administered Evans blue dye (Near-Infrared) labeled Ex-DC@CQDs and DC@CQDs [60]. This administration took place after the tumors had reached a volume of 200 to 300 mm^3. In order to track the distribution of the developed formulation, IVIS imaging was performed at designated time points before and after IV administration of formulation containing DC equivalent to 10 mg/kg, along with Evans-labeled Ex-DC@CQDs and DC@CQDs. Fluorescence images of the mice were captured at different

Table 2

Pharmacokinetic parameters of DC in mouse serum after single IV administration of Ex-DC@CQDs formulations at a dosage of 10 mg/kg DC. All data are expressed as mean ± SD ($n = 6$).

Parameter	DC		
	Free DC	DC@CQDs	Ex-DC@CQDs
C_{max} (μg/mL)	42.27 ± 5.21	47.045 ± 5.41	54.187 ± 8.11
$t_{1/2}$ (h)	1.01 ± 1.24	9.21 ± 1.41	16.88 ± 1.01
$AUC_0.\alpha$ (μg/mL*h)	90.5 ± 120.34	325.1 ± 114.12	1169.6 ± 121.21
V_{ss} (mL)	0.174 ± 0.021	0.322 ± 0.0045	0.406 ± 0.022
Cl (mL h^{-1})	0.11 ± 0.0061	0.03 ± 0.002	8.510 ± 0.002
MRT (h)	1.646 ± 1.12	10.05 ± 3.12	24.003 ± 3.40

Table 3

Pharmacokinetic parameters of AIC (metabolite) in mouse serum after single IV administration of Ex-DC@CQDs formulations at a dosage of 10 mg/kg DC. All data are expressed as mean ± SD ($n = 6$).

Parameter	AIC		
	Free DC	DC@CQDs	Ex-DC@CQDs
C_{max} (μg/mL)	2.15 ± 0.25	1.78 ± 0.11	1.95 ± 0.24
$t_{1/2}$ (h)	1.408 ± 0.93	13.79 ± 0.82	17.99 ± 0.95
$AUC_0.\alpha$ (μg/mL*h)	4.964 ± 20.34	9.342 ± 11.02	19.47 ± 11.01
V_{ss} (mL)	4.019 ± 0.044	13.04 ± 0.0032	9.512 ± 0.072
Cl (mL h^{-1})	2.015 ± 0.0033	1.07 ± 0.004	0.514 ± 0.001
MRT (h)	1.994 ± 1.02	15.95 ± 1.11	21.52 ± 1.04

time intervals (6, 12, and 24 h), and the deposition of Ex-DC@CQDs at the tumor site was assessed by quantifying the fluorescence intensity within a defined region of interest.

After 12 h of injection, a significant and sustained increase in fluorescence intensity was observed in the Exo-specific HSPG receptor targeted group (Ex-DC@CQDs) at the tumor site, which remained consistent for up to 24 h (Fig. 6, A-B). This finding highlights the superior localization of the Exo-specific HSPG receptor-targeted group (Ex-DC@CQDs) in the tumor tissue compared to the DC@CQDs groups. The effectiveness of the targeted formulation in achieving specific illumination of tumor tissue with a significant contrast can be attributed to the internalization process mediated by Exo and driven by the HSPG receptors [12,61]. In contrast, the relatively weak fluorescence observed at the tumor site for non-targeted nanoparticles (DC@CQDs) and the higher fluorescence signal in other organs can be attributed to their lack of targeting capability and systemic distribution [62]. Furthermore, the confirmation of these findings was obtained through *ex vivo* imaging of the tumor tissue and major organs collected from the sacrificed animals 24 h post-injection. The investigation of fluorescence intensity differences between the groups treated with targeted and non-targeted formulations was conducted by analyzing the differential distribution of formulation. Additionally, it was also found that the non-targeted group had a higher fluorescence intensity in the liver tissue than the targeted group, which indicates that the targeted formulation demonstrated an extended duration of circulation in the bloodstream and the target-specific drug delivery at the tumor site (Fig. 6, C-E). The aforementioned results were consistent with the outcomes of our *In vivo* pharmacokinetic study, providing further confirmation. Thus, Ex-DC@CQDs have been proven to have the ability to target the TME in which overexpressed cancer-derived Exo-specific receptors are present.

3.12. Pharmacokinetic and tissue drug distribution study

To study the effect of Ex-DC@CQDs on the pharmacokinetics and biodistribution of DC, mice with tumors were administered free DC, DC@CQDs, and Ex-DC@CQDs *via* IV injection at a dose of 10 mg/kg through the tail vein. The serum distribution profile over 24 h is presented in Fig. 7, panels A and B, while Tables 2 and 3 provide a summary of the pharmacokinetic parameters obtained through non-

compartmental modeling. As DC is a drug known for its rapid distribution to organs and subsequent conversion into an active metabolite, its serum concentration was observed to be consistently low in all the groups. The precursor ions were obtained at 183.20, 127.10, and 195.10 for DC, AIC, and Caffeine (IS), respectively, with a retention time between 2 and 4 min, while product ions were 166.10, 110.20, and 138.10 (Fig. S5). This observation aligns with previously published reports, confirming the consistency of this finding [63]. Furthermore, the administration of DC encapsulated in CQDs resulted in a distinct profile in both organs and serum over a 24 h period, differing from that of free drugs alone. Notably, the groups treated with Ex-DC@CQDs exhibited substantial increases in AUC0-∞ compared to both free DC and DC@CQDs. Specifically, the Ex-DC@CQDs group demonstrated a 12.92-fold increase in AUC0-∞ compared to free DC, and a 3.6-fold increase compared to DC@CQDs. The average half-life ($t_{1/2}$) of Ex-DC@CQDs was significantly longer, being 16.71 times greater than that of the free drug. Additionally, the mean residence time (MRT) was prolonged, with Ex-DC@CQDs displaying MRT values that were 14.58 times longer than free DC and 2.39 times longer than DC@CQDs, respectively (as presented in Tables 2 and 3). These findings strongly support that Ex-DC@CQDs exhibit an extended residence time within the body, potentially leading to improved accumulation at the tumor site through active targeted delivery and the EPR effect. Further, Ex-DC@CQDs demonstrated remarkable targeting efficiency expressed in terms of the Drug Targeting Index (DTI) for Ex-DC@CQDs surpassing both free drugs (17.32%) and DC@CQDs (2.66%) and signifying a pivotal advancement in drug delivery precision. Analytical method development of DC and AIC by LCMS is shown in Fig. S5. In light of the results, a significant difference was observed in the pharmacokinetic parameters between DC@CQDs and Ex-DC@CQDs. Ex-DC@CQDs were found to have higher AUC, MRT, and $t_{1/2}$ values than DC@CQDs, which can be attributed to the surface morphology, higher biocompatibility, and targeting aspects of Ex-DC@CQDs. Previous reports revealed that nanoparticles with an Exo coating and a target-specific surface decoration demonstration decreased opsonization properties, which eventually leads to an extended duration of circulation in the bloodstream [64,65]. During this study, it was also noted that the DC converts into their active metabolite AIC, which was also supported by previously published articles [46]. The conversion of DC to AIC was also estimated in serum as well as tissue distribution (Fig. 7 and Tables 2 and 3) and interestingly it was found that the earlier time points in free DC treated groups showed a higher conversion rate compared to the Ex-DC@CQDs treated group (Fig. 7B) which may be ascribed to the fact that DC encapsulated in the formulation would not be available to the liver enzyme. However, at the tumor site, the Ex-DC@CQDs treated groups showed higher AIC concentrations compared to free drug and non-targeted CQDs.

Ex-DC@CQD accumulation in tumor tissue has shown significant effects in terms of promoting DC and AIC delivery. After 24 h, the accumulation of Ex-DC@CQDs produced 3.1- and 4.5 times higher concentrations of DC and converted AIC, respectively, compared to free DC (Fig. 7 and Tables 2 and 3) [63]. When administered, DC undergoes enzymatic conversion in the liver, resulting in its immediate transformation into AIC. As a consequence of this metabolic process, the C_{max} of free DC is lower in comparison to that of Ex-DC@CQDs. As a matter of fact, Exo isolated from cancer cells possess an enzyme (CYP) in a very high concentration required for the drug conversion into a metabolite. The presence of higher concentrations of AIC in tumor tissue in the Ex-DC@CQDs treated groups suggested that this could be due to the presence of a metabolizing enzyme in Exo, which gets activated after reaching to tumor site and triggering an active metabolite formation. BC cell-derived Exo facilitate the cytochrome enzymes, particularly CYP1A1, CYP1A2, and CYP2E1 (Fig. 1K), that activate DC specifically within cancer cells due to the TME and thereby preserve the higher concentration of AIC inside the tumor cells while sparing other cells [63]. Because the above phenomenon requires further investigation, our group is working to reveal the detailed mechanism for cancer cell-
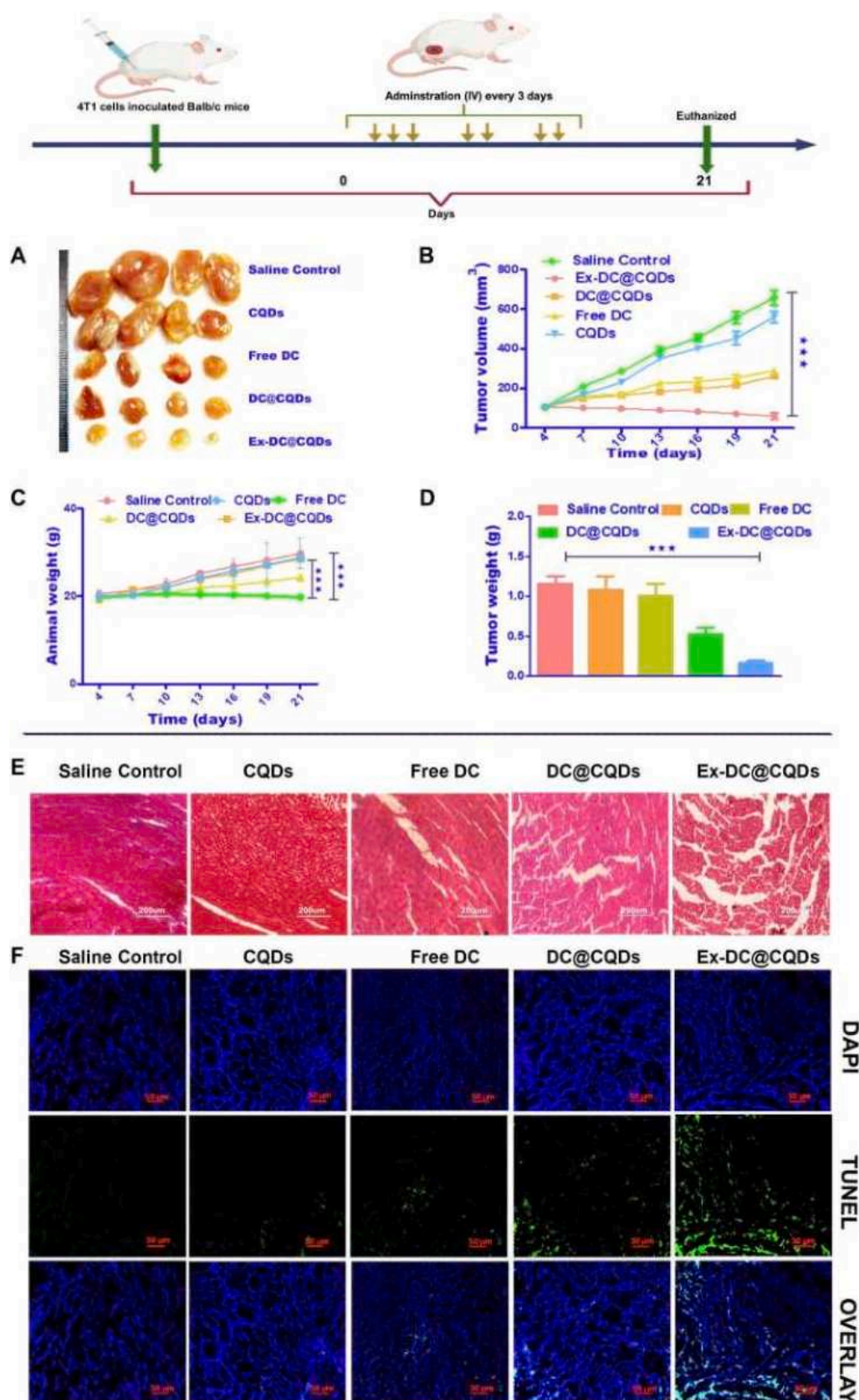
Fig. 8. *In vivo* tumor regression study against 4 T1 cells induced mammary tumor in Balb/c mice treated with DC (10 mg/kg). (A) Photographic representation of tumor morphology and shape observed at the end of the study. (B) The mean tumor growth curve at various time points of the study ($n = 6$). (C) The animal body weight monitored during treatment; the results are presented as mean ± standard deviation ($n = 6$). (D) Weights of excised tumors at the end of the tumor regression study. (E) Histological tumor tissue sections stained with H&E after 21 days of treatment. (F) TUNEL assay of tumor tissue sections from 4 T1 tumor associated Balb/c mice treated with different regimens for 21 days. The values are presented as mean ± standard deviation ($n = 6$).

isolated Exo-based drug conversion into a metabolite. The above outcome can also be supported by the lower MRT, and half-life of the free DC treated group in contrast to the Ex-DC@CQDs treated group with the rapid distribution of the free drug to the organs and rapid elimination by the kidney, which resulted in the lower concentration in blood.

3.13. Tumor regression studies

In this study, we investigated the anti-cancer properties of Ex-DC@CQDs using an aggressive 4 T1 subcutaneously implanted Balb/c mouse model. After the tumor volume reached 100–110 mm^3 in each animal, the mice were segregated into five groups: (I) PBS, (II) CQDs, (III) free DC, (IV) DC@CQDs, and (V) Ex-DC@CQDs. A drug dose equivalent to 10 mg/kg (for DC, DC@CQDs, and Ex-DC@CQDs) was administered IV as a bolus on days 0, 4, 7, 10, 13, 16, and 19 of the study. In order to investigate treatment-driven kinetics behind the cancer progression, tumor burden was measured with a Vernier caliper prior to each administration and calculated as [$\pi/6$ x (L) x (W)^2]. The observation revealed that the tumor burden of the Saline treated group increased rapidly within 3 days after injection. On the contrary, the groups that were administered the free drug experienced a slight decrease in tumor growth, likely due to limited bioavailability (Fig. 8D). Moreover, the administration of Ex-DC@CQDs exhibited a significantly more potent capability in suppressing the tumor progression, which indicated the enhanced bioavailability of DC as the result of Exo-specific HSPG-mediated targeting. In terms of quantitative analysis, the final tumor volume of Ex-DC@CQDs was found to be significantly lower compared to the control group ($p \leq 0.01$), free DC group ($p \leq 0.01$), and DC@CQDs group. Specifically, the tumor volume of Ex-DC@CQDs was 10.9, 4.8, and 4.3 times lower than in the saline control, free DC, and DC@CQDs groups, respectively. These results provide clear evidence of the superior therapeutic efficacy achieved with the Ex-DC@CQDs and DC@CQDs formulations when compared to the free DC and saline control groups.

Furthermore, at the end of the study, the excised tumor weight in the Ex-DC@CQDs treated group was found to be 7.25-fold, 6.25-fold, and 3.25-fold lower than that of the saline control, free DC, and DC@CQDs groups, respectively. These results align with the findings observed for tumor volume (Fig. 8B), indicating a consistent outcome and further supporting the efficacy of Ex-DC@CQDs treatment. The photographic representation of the harvested tumors presented in (Fig. 8A) further supports the findings, providing strong corroborating evidence consistent with the *in vitro* cytotoxicity results. Additionally, in order to assess the safety of the formulations, the body weight of the mice was monitored. As shown in Fig. 8C, the group treated with free DC experienced notable weight loss compared to the other groups. On the other hand, it was observed that the group treated with CQDs alone exhibited both increased efficacy and good tolerability, as indicated by a similar increase in body weight compared to the control group.

Therefore, the enhanced antitumor efficacy of Ex-DC@CQDs was attributed to the superior pharmacokinetic profile and higher tumor accumulation resulting from Exo-mediated HSPG receptor-driven cell uptake, as well as the sustained release nature of the carrier-mediated intracellular drug release.

3.14. Histology

To examine the potential toxicity of the formulation treatment *in vivo*, a histological analysis was done following the staining of the tissue sections with eosin, hematoxylin, and a TUNEL assay kit (Fig. 8, E-F). The treatment-based superior apoptotic effect was observed in the Ex-DC@CQDs treated group, indicating the efficacy of the treatment therapy (Fig. 8F). Additionally, the tumor treated with Ex-DC@CQDs exhibited a disorganized and disrupted morphology in comparison to the control and other treatment groups. This can be attributed to the higher concentration of the drug and its effective suppression of tumor growth.

4. Conclusion

In the present study, we have successfully developed an exosome-derived bioengineered quantum dots-based system to address the issue of complicated imprecise targeting that often leads to clinical toxicity with breast cancer therapy. We devised a strategy that involved loading DC into Fucose-based CQDs, which were then coated with cancer cell isolated Exo, resulting in Ex-DC@CQDs. The studies confirmed the formation and characteristics of the CQDs and demonstrated that the Exo retained their structural and functional properties within the system. The use of Exo facilitated the targeted delivery of the DC@CQDs to cancer cells through HSPG receptors, thereby enhancing therapeutic efficacy. The study showed that Ex-DC@CQDs exhibited precise targeting and increased cellular uptake, and induced cell death in BC cells through the generation of ROS, depolarization of MMP, and apoptosis. *In vivo* imaging demonstrated sustained fluorescence intensity at the tumor site, indicating efficient targeting through the exosome-mediated HSPG receptor-driven cell uptake. Additionally, the study evaluated the pharmacokinetic profile and antitumor efficacy of Ex-DC@CQDs compared to free DC and DC@CQDs. The results revealed a significant increase in the AUC$_{0-\infty}$ and a substantial reduction in tumor weight in the Ex-DC@CQDs-treated group, indicating improved pharmacokinetics, higher tumor accumulation, and sustained release of the carrier. Overall, our findings feature the potential of exosome-specific targeting and DC@CQD-mediated delivery as an effective intervention for BC. The use of Exo as nanocarriers offers advantages such as precise targeting, enhanced therapeutic efficacy, and reduced toxicity, facilitating the development of a new approach to biologically sourced nanocarriers for cancer targeting.

CRediT authorship contribution statement

Pratiksha Tiwari: Writing – review & editing, Writing – original draft, Visualization, Validation, Software, Methodology, Investigation, Formal analysis, Data curation, Conceptualization. **Ravi Prakash Shukla:** Writing – review & editing, Validation, Formal analysis, Data curation. **Krishna Yadav:** Writing – review & editing, Validation, Formal analysis. **Neha Singh:** Methodology. **Disha Marwaha:** Validation, Software. **Shalini Gautam:** Writing – review & editing. **Avijit Kumar Bakshi:** Formal analysis. **Nikhil Rai:** Data curation. **Ankit Kumar:** Methodology. **Deepak Sharma:** Software, Formal analysis. **Prabhat Ranjan Mishra:** Writing – review & editing, Visualization, Validation, Supervision, Resources, Funding acquisition, Formal analysis, Conceptualization.

Declaration of Competing Interest

None.

Data availability

Data will be made available on request.

number for this manuscript is 10693.

Appendix A. Supplementary data

Supplementary data to this article can be found online at https://doi.org/10.1016/j.jconrel.2023.11.005.

References

[1] S.H. Jafari, Z. Saadatpour, A. Salmaninejad, F. Momeni, M. Mokhtari, J.S. Nahand, M. Rahmati, H. Mirzaei, M. Kianmehr, Breast cancer diagnosis: imaging techniques and biochemical markers, J. Cell. Physiol. 233 (2018) 5200–5213, https://doi.org/10.1002/jcp.26379.

[2] M. Sharma, A.K. Bakshi, N. Mittapelly, S. Gautam, D. Marwaha, N. Rai, N. Singh, P. Tiwari, N. Agarwal, A. Kumar, P.R. Mishra, Recent updates on innovative approaches to overcome drug resistance for better outcomes in cancer, J. Control. Release 346 (2022) 43–70, https://doi.org/10.1016/J.JCONREL.2022.04.007.

[3] K.E. Gilligan, R.M. Dwyer, Engineering exosomes for cancer therapy, Int. J. Mol. Sci. 18 (2017), https://doi.org/10.3390/ijms18061122.

[4] P. Tiwari, K. Yadav, R.P. Shukla, S. Gautam, D. Marwaha, M. Sharma, P.R. Mishra, Surface modification strategies in translocating nano-vesicles across different barriers and the role of bio-vesicles in improving anticancer therapy, J. Control. Release 363 (2023) 290–348, https://doi.org/10.1016/j.jconrel.2023.09.016.

[5] Y. Wang, T. Huo, H. Jiang, Y. Xie, X. Zhang, H. Nie, Y. Yang, M. Qian, W. Li, T. Hao, W. Guo, Y. Qin, J. Shi, W. Shi, R. Huang, Sugar-originated carbon nanodots selectively damage the tumor and enhance the sensitivity of chemotherapy, Nano Today 38 (2021), 101200, https://doi.org/10.1016/j.nantod.2021.101200.

[6] J. Pardo, Z. Peng, R.M. Leblanc, Cancer targeting and drug delivery using Carbon-based quantum dots and nanotubes, Molecules. 23 (2018), https://doi.org/10.3390/molecules23020378.

[7] A.A. Al-Badr, M.M. Alodhaib, Dacarbazine, in: Profiles Drug Subst. Excipients Relat. Methodol., 2016, pp. 323–377, https://doi.org/10.1016/bs.podrm.2015.12.002.

[8] R.N.-B. Tagne, Compositions and Methods for Treating cancer with Dacarbazine Nanoemulsions, 2008.

[9] C.H. Barrios, Global challenges in breast cancer detection and treatment, Breast 62 (2022) S3–S6, https://doi.org/10.1016/j.breast.2022.02.003.

[10] K. Yadav, D. Singh, M.R. Singh, Novel archetype in psoriasis management bridging molecular dynamics in exploring novel therapies, Eur. J. Pharmacol. 907 (2021), 174254, https://doi.org/10.1016/j.ejphar.2021.174254.

[11] D. Barbouri, N. Afratis, C. Gialeli, D.H. Vynios, A.D. Theocharis, N.K. Karamanos, Syndecans as modulators and potential pharmacological targets in cancer progression, Front. Oncol. 4 (2014) 4, https://doi.org/10.3389/fonc.2014.00004.

[12] H.C. Christianson, K.J. Svensson, T.H. van Kuppevelt, J.-P. Li, M. Belting, Cancer cell exosomes depend on cell-surface heparan sulfate proteoglycans for their internalization and functional activity, Proc. Natl. Acad. Sci. U. S. A. 110 (2013) 17380–17385, https://doi.org/10.1073/pnas.1304266110.

[13] H. Lin, J. Huang, L. Ding, Preparation of Carbon dots with high-fluorescence quantum yield and their application in dopamine fluorescence probe and cellular imaging, J. Nanomater. 2019 (2019), https://doi.org/10.1155/2019/5037243.

[14] Y. Zhao, S. Zuo, M. Miao, The effect of oxygen on the microwave-assisted synthesis of carbon quantum dots from polyethylene glycol, RSC Adv. 7 (2017) 16637–16643, https://doi.org/10.1039/C7RA01804E.

[15] H. Zhu, X. Wang, Y. Li, Z. Wang, F. Yang, X. Yang, Microwave synthesis of fluorescent carbon nanoparticles with electrochemiluminescence properties, Chem. Commun. (2009) 5118–5120, https://doi.org/10.1039/B907612C.

[16] J.-L. Ma, B.-C. Yin, X. Wu, B.-C. Ye, Simple and cost-effective glucose detection based on carbon nanodots supported on silver nanoparticles, Anal. Chem. 89 (2017) 1323–1328, https://doi.org/10.1021/acs.analchem.6b04259.

[17] K. Yadav, D. Singh, M.R. Singh, Development and characterization of corticosteroid loaded lipid carrier system for psoriasis, Res. J. Pharm. Technol. 14 (2021) 966–970, https://doi.org/10.5958/0974-360X.2021.00172.4.

[18] W. Su, R. Guo, F. Yuan, Y. Li, X. Li, Y. Zhang, S. Zhou, L. Fan, Red-emissive carbon quantum dots for nuclear drug delivery in cancer stem cells, J. Phys. Chem. Lett. 11 (2020) 1357–1363, https://doi.org/10.1021/acs.jpclett.9b03891.

[19] F.A. Khan, N. Lammari, A.S. Muhammad Siar, K.M. Alkhater, S. Asiri, S. Akhtar, I. Almansour, W. Alamoudi, W. Haroun, W. Louaer, A.H. Meniai, A. Elaissari, Quantum dots encapsulated with curcumin inhibit the growth of colon cancer, breast cancer and bacterial cells, Nanomedicine. 15 (2020) 969–980, https://doi.org/10.2217/nnm-2019-0429.

[20] I. Kimiz-Gebologlu, S.S. Oncel, Exosomes: large-scale production, isolation, drug loading efficiency, and biodistribution and uptake, J. Control. Release 347 (2022) 533–543, https://doi.org/10.1016/j.jconrel.2022.05.027.

[21] Y. Risha, Z. Minic, S.M. Ghobadloo, M.V. Berezovski, The proteomic analysis of breast cell line exosomes reveals disease patterns and potential biomarkers, Sci. Rep. 10 (2020) 13572, https://doi.org/10.1038/s41598-020-70393-4.

[22] S. Keerthikumar, D. Chisanga, D. Ariyaratne, H. Al Saffar, S. Anand, K. Zhao, M. Samuel, M. Pathan, M. Jois, N. Chilamkurti, L. Gangoda, S. Mathivanan, ExoCarta: a web-based compendium of exosomal cargo, J. Mol. Biol. 428 (2016) 688–692, https://doi.org/10.1016/j.jmb.2015.09.019.

[23] R.P. Shukla, S. Urandur, V.T. Banala, D. Marwaha, S. Gautam, N. Rai, N. Singh, P. Tiwari, P. Shukla, P.R. Mishra, Development of putrescine anchored nano-crystalsomes bearing doxorubicin and oleanolic acid: deciphering their role in

[24] K. Yadav, D. Singh, M.R. Singh, Nanovesicles delivery approach for targeting steroid mediated mechanism of antipsoriatic therapeutics, J. Drug Deliv. Sci. Technol. 65 (2021), 102688, https://doi.org/10.1016/j.jddst.2021.102688.

[25] G. Pandey, N. Mittapelly, G.R. Valicherla, R.P. Shukla, S. Sharma, V.T. Banala, S. Urandur, A.K. Jajoriya, K. Mitra, D.P. Mishra, J.R. Gayen, P.R. Mishra, P-gp modulatory acetyl-11-keto-β-boswellic acid based nanoemulsified carrier system for augmented oral chemotherapy of docetaxel, Colloids Surf. B: Biointerfaces 155 (2017) 276–286, https://doi.org/10.1016/j.colsurfb.2017.04.028.

[26] S. Urandur, V.T. Banala, R.P. Shukla, N. Mittapelly, G. Pandey, N. Kalleti, K. Mitra, S.K. Rath, R. Trivedi, P. Ramarao, P.R. Mishra, Anisamide-anchored lyotropic nano-liquid crystalline particles with AIE effect: a smart optical beacon for tumor imaging and therapy, ACS Appl. Mater. Interfaces 10 (2018) 12960–12974, https://doi.org/10.1021/ACSAMI.7B19109/ASSET/IMAGES/LARGE/AM-2017-19109Y_0004.JPEG.

[27] S. Urandur, V.T. Banala, R.P. Shukla, S. Gautam, D. Marwaha, N. Rai, M. Sharma, S. Sharma, P. Ramarao, P.R. Mishra, Theranostic lyotropic liquid crystalline nanostructures for selective breast cancer imaging and therapy, Acta Biomater. 113 (2020) 522–540, https://doi.org/10.1016/j.actbio.2020.06.023.

[28] S. Sharma, J. Singh, A. Verma, B.V. Teja, R.P. Shukla, S.K. Singh, V. Sharma, R. Konwar, P.R. Mishra, Hyaluronic acid anchored paclitaxel nanocrystals improves chemotherapeutic efficacy and inhibits lung metastasis in tumor-bearing rat model, RSC Adv. 6 (2016) 73083–73095, https://doi.org/10.1039/C6RA11260A.

[29] S. Gautam, D. Marwaha, N. Singh, N. Rai, M. Sharma, P. Tiwari, S. Urandur, R. Shukla, V. Teja, P. Mishra, Self-assembled redox-sensitive polymeric nanostructures facilitate the intracellular delivery of paclitaxel for improved breast cancer therapy, Mol. Pharm. 20 (2023), https://doi.org/10.1021/acs.molpharmaceut.2c00673.

[30] S. Sharma, A. Verma, J. Singh, B.V. Teja, N. Mittapelly, G. Pandey, S. Urandur, R.P. Shukla, R. Konwar, P.R. Mishra, Vitamin B6 tethered endosomal pH responsive lipid nanoparticles for triggered intracellular release of doxorubicin, ACS Appl. Mater. Interfaces 8 (2016) 30407–30421, https://doi.org/10.1021/ACSAMI.6B08958.

[31] V. Teja, S. Urandur, S. Sharma, M. Sharma, R. Shukla, D. Marwaha, S. Gautam, M. Sharma, P. Mishra, Targeted co-delivery of aldose reductase inhibitor epalrestat and chemotherapeutic doxorubicin via redox-sensitive prodrug approach promotes synergistic tumor suppression, Biomater. Sci. 7 (2019), https://doi.org/10.1039/C9BM00221A.

[32] V.T. Banala, S. Sharma, P. Barnwal, S. Urandur, R.P. Shukla, N. Ahmad, N. Mittapelly, G. Pandey, M. Dwivedi, N. Kalleti, K. Mitra, S.K. Rath, R. Trivedi, P.R. Mishra, Synchronized ratiometric codelivery of metformin and topotecan through engineered nanocarrier facilitates In vivo synergistic precision levels at tumor site, Adv. Healthc. Mater. 7 (2018), https://doi.org/10.1002/ADHM.201800300.

[33] D. Marwaha, S. Gautam, N. Singh, N. Rai, M. Sharma, P. Tiwari, R. Shukla, S. Urandur, V. Teja, M. Nilakanth, A. Kumar, P. Mishra, Synergistic delivery of Imatinib through multifunctional nano-crystalline capsules, in response to redox environment for improved breast cancer therapy, Colloids Surf. B: Biointerfaces 226 (2023), 113316, https://doi.org/10.1016/j.colsurfb.2023.113316.

[34] R.P. Shukla, J. Dewangan, S. Urandur, V.T. Banala, M. Diwedi, S. Sharma, S. Agrawal, S.K. Rath, R. Trivedi, P.R. Mishra, Multifunctional hybrid nanoconstructs facilitate intracellular localization of doxorubicin and genistein to enhance apoptotic and anti-angiogenic efficacy in breast adenocarcinoma, Biomater. Sci. 8 (2020) 1298–1315, https://doi.org/10.1039/C9BM01246J.

[35] Y. Liu, W. Zhang, Y. Yang, Validated hydrophilic interaction LC–MS/MS method for simultaneous quantification of dacarbazine and 5-amino-4-imidazole-carboxamide in human plasma, Talanta. 77 (2008) 412–421, https://doi.org/10.1016/j.talanta.2008.07.004.

[36] Y. Choi, N. Thongsai, A. Chae, S. Jo, E.B. Kang, P. Paoprasert, S.Y. Park, I. In, Microwave-assisted synthesis of luminescent and biocompatible lysine-based carbon quantum dots, J. Ind. Eng. Chem. 47 (2017) 329–335, https://doi.org/10.1016/j.jiec.2016.12.002.

[37] T.V. de Medeiros, J. Manioudakis, F. Noun, J.-R. Macairan, F. Victoria, R. Naccache, Microwave-assisted synthesis of carbon dots and their applications, J. Mater. Chem. C 7 (2019) 7175–7195, https://doi.org/10.1039/C9TC01640F.

[38] Q. Zeng, D. Shao, X. He, Z. Ren, W. Ji, C. Shan, S. Qu, J. Li, L. Chen, Q. Li, Carbon dots as a trackable drug delivery carrier for localized cancer therapy in vivo, J. Mater. Chem. B 4 (2016) 5119–5126, https://doi.org/10.1039/C6TB01259K.

[39] L. Rao, G.-T. Yu, Q.-F. Meng, L.-L. Bu, R. Tian, L.-S. Lin, H. Deng, W. Yang, M. Zan, J. Ding, A. Li, H. Xiao, Z.-J. Sun, W. Liu, X. Chen, Cancer cell membrane-coated nanoparticles for personalized therapy in patient-derived xenograft models, Adv. Funct. Mater. 29 (2019) 1905671, https://doi.org/10.1002/adfm.201905671.

[40] H. Sun, J. Su, Q. Meng, Q. Yin, L. Chen, W. Gu, Z. Zhang, H. Yu, P. Zhang, S. Wang, Y. Li, Cancer cell membrane-coated gold nanocages with hyperthermia-triggered drug release and homotypic target inhibit growth and metastasis of breast cancer, Adv. Funct. Mater. 27 (2017) 1604300, https://doi.org/10.1002/adfm.201604300.

[41] M. Sharifi, W.C. Cho, A. Ansariesfahani, R. Tarharoudi, H. Malekisarvar, S. Sari, S. H. Bloukh, Z. Edis, M. Amin, J.P. Gleghorn, T.L.M. Ten Hagen, M. Falahati, An updated review on EPR-based solid tumor targeting nanocarriers for cancer treatment, Cancers (Basel) 14 (2022), https://doi.org/10.3390/cancers14122868.

[42] M.K. Rasmussen, J.N. Pedersen, R. Marie, Size and surface charge characterization of nanoparticles with a salt gradient, Nat. Commun. 11 (2020) 2337, https://doi.org/10.1038/s41467-020-15889-3.

[43] S. Gunasekaran, S. Kumaresan, R. Arunbalaji, G. Anand, S. Srinivasan, Density functional theory study of vibrational spectra, and assignment of fundamental modes of dacarbazine, J. Chem. Sci. 120 (2008) 315–324, https://doi.org/10.1007/s12039-008-0054-8.

[44] N. Papaioannou, A. Marinovic, N. Yoshizawa, A.E. Goode, M. Fay, A. Khlobystov, M.-M. Titirici, A. Sapelkin, Structure and solvents effects on the optical properties of sugar-derived carbon nanodots, Sci. Rep. 8 (2018) 6559, https://doi.org/10.1038/s41598-018-25012-8.

[45] X. Wang, L. Tian, J. Lu, I.O.-L. Ng, Exosomes and cancer - diagnostic and prognostic biomarkers and therapeutic vehicle, Oncogenesis. 11 (2022) 54, https://doi.org/10.1038/s41389-022-00431-5.

[46] J.M. Reid, M.J. Kuffel, J.K. Miller, R. Rios, M.M. Ames, Metabolic activation of dacarbazine by human cytochromes P450: the role of CYP1A1, CYP1A2, and CYP2E1, Clin. Cancer Res. 5 (1999) 2192–2197.

[47] C. Ding, Z. Li, A review of drug release mechanisms from nanocarrier systems, Mater. Sci. Eng. C 76 (2017) 1440–1453, https://doi.org/10.1016/j.msec.2017.03.130.

[48] R. Li, Y. Xie, Nanodrug delivery systems for targeting the endogenous tumor microenvironment and simultaneously overcoming multidrug resistance properties, J. Control. Release 251 (2017) 49–67, https://doi.org/10.1016/j.jconrel.2017.02.020.

[49] M.A. Rahman, V. Mittal, S. Wahab, A. Alsayari, A. Bin Muhsinah, D. Almaghaslah, Intravenous nanocarrier for improved efficacy of quercetin and curcumin against breast cancer cells: development and comparison of single and dual drug-loaded formulations using hemolysis, cytotoxicity and cellular uptake studies, Membranes (Basel). 12 (2022), https://doi.org/10.3390/membranes12070713.

[50] A. Gonda, J. Kabagwira, G.N. Senthil, N.R. Wall, Internalization of exosomes through receptor-mediated endocytosis, Mol. Cancer Res. 17 (2019) 337–347, https://doi.org/10.1158/1541-7786.MCR-18-0891.

[51] J.J. Rennick, A.P.R. Johnston, R.G. Parton, Key principles and methods for studying the endocytosis of biological and nanoparticle therapeutics, Nat. Nanotechnol. 16 (2021) 266–276, https://doi.org/10.1038/s41565-021-00858-8.

[52] H. Park, M. Kim, H.-J. Kim, Y. Lee, Y. Seo, C.D. Pham, J. Lee, S.J. Byun, M.-H. Kwon, Heparan sulfate proteoglycans (HSPGs) and chondroitin sulfate proteoglycans (CSPGs) function as endocytic receptors for an internalizing anti-nucleic acid antibody, Sci. Rep. 7 (2017) 14373, https://doi.org/10.1038/s41598-017-14793-z.

[53] J.L. Munoz, N.D. Walker, K.W. Scotto, P. Rameshwar, Temozolomide competes for P-glycoprotein and contributes to chemoresistance in glioblastoma cells, Cancer Lett. 367 (2015) 69–75, https://doi.org/10.1016/j.canlet.2015.07.013.

[54] E.Z. Lapkina, A.R. Esimbekova, V.D. Beleniuk, A.A. Savchenko, T.G. Ruksha, The distribution of B16 melanoma cells in cell-cycle phases under the influence of

[55] dacarbazine, Cell Tissue Biol. 17 (2023) 161–168, https://doi.org/10.1134/S1990519X23020104.

[56] S. Şimşek, A.A. Şüküroğlu, D. Yetkin, B. Özbek, D. Battal, R. Genç, DNA-damage and cell cycle arrest initiated anti-cancer potency of super tiny carbon dots on MCF7 cell line, Sci. Rep. 10 (2020) 1–14, https://doi.org/10.1038/s41598-020-70796-3.

[57] T.-H. Ku, W.-T. Shen, C.-T. Hsieh, G.S. Chen, W.-C. Shia, Specific forms of graphene quantum dots induce apoptosis and cell cycle arrest in breast cancer cells, Int. J. Mol. Sci. 24 (2023), https://doi.org/10.3390/ijms24044046.

[58] C.J. Norbury, B. Zhivotovsky, DNA damage-induced apoptosis, Oncogene. 23 (2004) 2797–2808, https://doi.org/10.1038/sj.onc.1207532.

[59] Y. Ding, J. Yu, X. Chen, S. Wang, Z. Tu, G. Shen, H. Wang, R. Jia, S. Ge, J. Ruan, K.W. Leong, X. Fan, R.O.S. Dose-Dependent Carbon-Dot-Induced, Promote uveal melanoma cell tumorigenicity via activation of mTOR signaling and glutamine metabolism, Adv. Sci. (Weinheim, Baden-Wurttemberg, Ger.) 8 (2021) 2002404, https://doi.org/10.1002/advs.202002404.

[60] S. Salunkhe, M. Dheeraj, D. Basak, A. Chitkara, Mittal, surface functionalization of exosomes for target-specific delivery and in vivo imaging & tracking: strategies and significance, J. Control. Release 326 (2020) 599–614, https://doi.org/10.1016/j.jconrel.2020.07.042.

[61] M. Zhang, S. Hu, L. Liu, P. Dang, Y. Liu, Z. Sun, B. Qiao, C. Wang, Engineered exosomes from different sources for cancer-targeted therapy, Signal Transduct. Target. Ther. 8 (2023) 124, https://doi.org/10.1038/s41392-023-01382-y.

[62] S. Li, W. Su, H. Wu, T. Yuan, C. Yuan, J. Liu, G. Deng, X. Gao, Z. Chen, Y. Bao, F. Yuan, S. Zhou, H. Tan, Y. Li, X. Li, L. Fan, J. Zhu, A.T. Chen, F. Liu, Y. Zhou, M. Li, X. Zhai, J. Zhou, Targeted tumour theranostics in mice via carbon quantum dots structurally mimicking large amino acids, Nat. Biomed. Eng. 4 (2020) 704–716, https://doi.org/10.1038/s41551-020-0540-y.

[63] C. Joukhadar, N. Klein, R.M. Mader, C. Schrolnberger, B. Rizovski, E. Heere-Ress, H. Pehamberger, N. Strauchmann, B. Jansen, M. Müller, Penetration of dacarbazine and its active metabolite 5-aminoimidazole-4-carboxamide into cutaneous metastases of human malignant melanoma, Cancer. 92 (2001) 2190–2196, https://doi.org/10.1002/1097-0142(20011015)92:8<2190::aid-cncr1562>3.0.co;2-2.

[64] Y. Tian, S. Li, J. Song, T. Ji, M. Zhu, G.J. Anderson, J. Wei, G. Nie, A doxorubicin delivery platform using engineered natural membrane vesicle exosomes for targeted tumor therapy, Biomaterials. 35 (2014) 2383–2390, https://doi.org/10.1016/j.biomaterials.2013.11.083.

[65] G. Cheng, W. Li, L. Ha, X. Han, S. Hao, Y. Wan, Z. Wang, F. Dong, X. Zou, Y. Mao, S.-Y. Zheng, Self-assembly of extracellular vesicle-like metal–organic framework nanoparticles for protection and intracellular delivery of biofunctional proteins, J. Am. Chem. Soc. 140 (2018) 7282–7291, https://doi.org/10.1021/jacs.8b03584.

Synchronized Ratiometric Codelivery of Metformin and Topotecan through Engineered Nanocarrier Facilitates In Vivo Synergistic Precision Levels at Tumor Site

Venkatesh Teja Banala, Shweta Sharma, Puja Barnwal, Sandeep Urandur, Ravi P. Shukla, Naseer Ahmad, Naresh Mittapelly, Gitu Pandey, Monika Dwivedi, Navodayam Kalleti, Kalyan Mitra, Srikanta Kumar Rath, Ritu Trivedi, and Prabhat Ranjan Mishra*

The combination of metabolic modulators with chemotherapy holds vast promise for effective inhibition of tumor progression and invasion. Herein, a ratiometric codelivery platform is developed for metformin (MET), a known metabolic modulator and topotecan (TPT), a chemotherapeutic drug, by engineering lipid bilayer–camouflaged mesoporous silica nanoparticles (LB-MSNs). In an attempt to deliver and maintain high tumor site concentrations of MET and TPT, a novel ion pairing–assisted loading procedure is developed using pamoic acid (PA) as an in situ trapping agent. PA, a hydrophobic counterion, increases the hydrophobicity of MET and TPT and facilitates MSNs with exceptionally high payload capacity (>40 and 32 wt%, respectively) and controlled release profile. Further, the synergy between MET and TPT determined by a modeling approach helps to afford synchronized delivery of both the drugs. Coloaded MET and TPT LB-MSNs present synergistic cytotoxicity against MDA-MB-231/4T1 cells and effectively promote apoptosis via mitochondrial membrane depolarization and cell cycle arrest. Extended pharmacokinetic profiles in preclinical models with fourfold to sevenfold longer circulation half-life and 7.5–100 times higher tumor site concentrations correspond to a significant increase in pharmacodynamic efficacy. Taken together, the developed codelivery approach effectively addresses the challenges in the chemotherapeutic efficacy of MET and TPT collectively.

1. Introduction

Conceding to the shortcomings of contemporary management stratagems, breast cancer exults as one of the most frequent and fatal malignances among women globally. Progressively more failures of surgical resection, radiotherapy, also hormone therapy, owing to the desensitization of receptors, had raised disquieting ultimatum. The clinical benefits of hormone therapy are limited due to the common issues like drug resistance, dose limited toxicity, and harsh tumor microenvironment that hinder the drug penetration and efficacy.[1] Thus, growing obligation in terms of complexity in treatment manifests the inception of hormone refractory breast cancer. Due to the physiological complexity of the tumor, monotherapy strategies are found to be not effective with more relapse rates which led to an interest in combination chemotherapy regimens, referring to the simultaneous administration of two or more drugs for achieving long-term prognosis with less unwanted side effects.[2] Unlike monotherapy, combination chemotherapies may cause synergistic response, maximize the therapeutic effect, and overcome drug resistance by modulating different signaling pathways in cancer cells. With the increase in understanding of molecular pathways, tumor microenvironment, and host–tumor interactions, new combination therapies are continuously evolving with new paradigms.[2b,3] Combination therapy with drugs that enable

V. T. Banala, Dr. S. Sharma, P. Barnwal, S. Urandur, R. P. Shukla, N. Mittapelly, G. Pandey, Dr. M. Dwivedi, Dr. P. R. Mishra
Division of Pharmaceutics and Pharmacokinetics
CSIR–Central Drug Research Institute
Lucknow 226031, India
E-mail: prabhat_mishra@cdri.res.in, mishrapr@hotmail.com
N. Ahmad, Dr. R. Trivedi
Division of Endocrinology
CSIR–Central Drug Research Institute
Lucknow 226031, India

N. Kalleti, Dr. S. K. Rath
Division of Toxicology
CSIR–Central Drug Research Institute
Lucknow 226031, India
Dr. K. Mitra
Electron Microscopy Division
CSIR–Central Drug Research Institute
Lucknow 226031, India

1800300 (1 of 14)

metabolic reprograming is one such approach gaining more clinical prominence in recent years by addressing chemoresistance and safety concerns tangled in standard chemotherapies.[4]

Recent studies have shown that metformin (MET), a common antidiabetic drug and promising anticancer metabolic modulator, demonstrated significant growth inhibition and proapoptotic effects in several cancers, including breast cancer.[5] MET activates 5′ adenosine monophosphate-activated protein kinase (AMPK), inhibits the mammalian target of rapamycin (mTOR), and downregulates excision repair cross-complementation group 1 (ERCC1).[6] Retrospective studies have reported that patients with diabetes receiving MET exhibited decreased cancer incidence and cancer-related mortality.[7] Various early stage clinical trials are presently underway to probe metformin's potential to combat an array of cancers, including colorectal, prostate, endometrial, and breast cancer.[5a] However, clinical progress of MET as a treatment regimen has been constrained by its rapid elimination, high aqueous solubility, and subtherapeutic tumor site concentrations.[8]

Interestingly, several preclinical studies have shown that MET exerts synergistic effects in combination with various classes of chemotherapeutic agents, like hormone modulation, antimetabolite, antibiotics, and drugs that affect structure and function of DNA.[9] Having realized that MET could show synergistic effects in combination with topoisomerase inhibitors,[10] in this study, we explored the combination therapy of MET with topotecan (TPT) against breast cancer. TPT is a semisynthetic analog of camptothecin suppressing DNA replication by inhibiting the nuclear enzyme topoisomerase I. TPT has been licensed to be a second line anticancer agent for small cell lung cancer (SCLC)[11] and ovarian cancer.[12] In addition to its cytotoxic activity against solid tumors, TPT has shown potential activity against metastases from breast cancer[13] and SCLC[14] in numerous clinical reports.

Theoretically, the success of combination chemotherapy in cancer majorly depends on the ratios of individual agents at the tumor site. Accounting to the dissimilar pharmacokinetic profiles of individual drugs, meager penetration, and heterogeneous distribution, the redemption of actual synergistic ratios at the target site confronted issues to realize the ultimate therapeutic effect of the regimen.[15] To mitigate the problems associated with free drug combination therapy, nanoparticles have formulated to coload synergistic drug combinations.[16] Delivery of synergistic drug ratios through nanocarriers provides controlled, temporal, and spatial delivery of multiple cargos, enables drug accumulation in tumor, and releases the drugs at a synchronized rate, thereby, probability of maintenance of intracellular synergistic drug concentrations is possible.[15c,17] But, coencapsulation of multiple drugs with different physicochemical properties in the same nanocarrier and controlling the drug release are always challenging tasks.[18] Appropriate physical- and chemical engineering of the nanoparticles are needed to enable optimal loading of multiple drugs and by imparting adjustable release kinetics to the delivery vehicle commensurate the required concentration–time profile at the site of action.[19]

Herein, we describe the coencapsulation of MET and TPT in a lipid bilayer–coated mesoporous silica nanoparticles (LB-MSNs) with an aim to achieve high payload and controlled release profile. Among candidate nanocarriers, MSNs offers many advantages over polymeric and lipidic delivery systems, such as uniform controlled particle size and shape with high surface area and modifiable surface chemistry which can widely accommodate high payloads of disparate cargos.[20] However, MSNs often require coatings to shield the surface silanol groups that are highly lipophilic and known to promote nonspecific binding and mononuclear phagocytic system (MPS) uptake.[21] In this context, lipid bilayer–coated MSNs have unique attributes which combine the advantages of liposomes with MSNs. To date, several studies reported the effective delivery of multiple classes of drugs and drug combinations using lipid bilayer–supported MSNs with excellent in vitro and in vivo results.[22] Since, MET is a highly water-soluble drug (>300 mg mL⁻¹), conventional polymeric and lipidic nanoparticulate systems fail in achieving reasonable payload efficiency. Our initial trials with PLGA nanoparticle could be able to accommodate less than 5% w/w of MET with rapid release within 8 h (data not shown). Although liposomal system exhibited efficient loading, inherent stability and burst release drawn obscure inferences for the liposomal system.[23] To overcome these challenges, we developed a novel hydrophobic ion trapping–assisted loading of MET and TPT using pamoic acid (PA) as in situ ion trapping agent. The large surface area of MSNs enables to achieve a high payload of both the drugs and in situ ion trapping offers reasonable hydrophobicity to MET, whereas, TPT exhibited protagonist for controlling the release. The in vitro synergy evaluation between MET and TPT using modeling approach is a major highlight of the study, where the derived ratiometric payload of drugs was delivered and evaluated for enhancement of total efficacy of plain drugs in comparison to the mixture of nanoparticles and coloaded nanoparticles. Additionally, pharmacokinetic studies and intratumoral drug concentrations were determined as a measure of maintenance of synergistic drug ratios and local drug bioavailability. The pharmacodynamic capability of the designed approach was evaluated in 4T1 tumor–bearing mouse model. Overall, this work illustrates the example of how to rationally design and coencapsulate highly water-soluble drugs with controlled release, how modifying the drug loading conditions can affect drug coencapsulation and provides insights on designing combination chemotherapy studies for assessing drug synergism in vitro and in vivo.

2. Results and Discussion

2.1. Coencapsulation of MET and TPT in Lipid Bilayer–Coated Mesoporous Silica Nanoparticles Using PA as In Situ Hydrophobic Ion Pairing (HIP) Agent

In this study, we have selected two water-soluble drugs, MET and TPT for the coencapsulation into the MSNs. Here, we took a major challenge to entrap highly water-soluble MET (>300 mg mL⁻¹) into the MSNs with an objective to control the release reasonably for a duration of 24–48 h. To achieve this goal, we have used PA as novel in situ hydrophobic ion trapping agent (HIP) for high drug loading and controlled release. To understand the HIP formation, metformin pamoate (MET-PA) and topotecan pamoate (TPT-PA) salts were synthesized and confirmed with ¹H-NMR (see the Supporting Information for a detailed discussion). From the equilibrium solubility experiments, it was clear

**ADVANCED
SCIENCE NEWS**
www.advancedsciencenews.com

**ADVANCED
HEALTHCARE
MATERIALS**
www.advhealthmat.de

that aqueous solubility of HIPs was ≈40-fold and ≈7.7-fold lower for MET-PA and TPT-PA, respectively, in comparison to plain drugs (Figure S1D,F, Supporting Information).

Although HIP formation is confirmed, one major challenge in loading MET is its low permeability across lipid bilayer due to its ionic nature and high pK_a (>12.4.). Based on various reports and evidences stating the ionic transport of drugs, we have performed transwell artificial membrane permeability assay for MET at different temperature and pH conditions.[24] It was observed that the effective permeability of MET was increased from fivefold to 28-fold with an increase in temperature and pH (Figure S2A1, Supporting Information). After understanding the positive effects of pH and temperature on the permeability of MET, we proceed to develop an active loading approach using PA as ion trapping agent. Initially, we have encapsulated MET and TPT individually into LB-MSNs. The passive entrapment of the MET and TPT into the cores of MSNs achieved a loading efficiency of 18 and 15 wt%, respectively. In our preliminary examination, it was found that plain MET-loaded MSNs could not sustain the drug release due to the high aqueous solubility. With an aim to load further high amount of drug with a controlled release, we have developed a novel remote loading technique. To the best of our knowledge, this is the first report of using in situ hydrophobic ion pairing for high drug loading of water-soluble drugs.

To develop remote loading procedure we used PA-loaded LB-MSNs, (PA)LB-MSNs, composed of SoyaPC/cholesterol/1,2-distearoyl-sn-glycero-3-phosphoethanolamine-polyethylene glycol-$_{2000}$ (DSPE-PEG$_{2000}$) at a molar ratio of 7:2.75:0.25 (**Figure 1**A). The (PA)LB-MSNs were incubated in 10 mg mL^{-1} of MET and 1 mg mL^{-1} of TPT drug solutions. The gradient and electrochemical potential across the lipid membrane and other factors like pH and incubation temperature allow the drug to drive inside the MSNs and get entrapped inside the pores as HIP after precipitating with the counterion, PA (Figure 1B). Different loading parameters were employed to achieve efficient loading. For MET, an optimum pH 9 was maintained outside the MSNs. Although MET exists in ionic form, pH 9 was selected to prevent the harsh environment. For TPT, being an amphipathic base pH 7.4 was found sufficient to maintain the gradient for the remote loading into MSNs. Under defined conditions, we able to achieve a maximum loading of ≈40 wt % for MET and ≈32 wt% for the TPT. The coloading was performed under the conditions of MET by which we have achieved around 35 wt% of MET and 10 wt% of TPT. For all the formulations, we have selected an optimum 4 h of incubation time for efficient loading.

Although we have achieved a maximum loading up to 35–40%, we have chosen to load 25% of MET and 0.5% of TPT based on efficient synergy achieved in in vitro modeling studies. To achieve 25/0.5 wt% ratio of loading, we have used 5 mg mL^{-1} of MET and 0.08 mg mL^{-1} of TPT solutions with triethylamine (TEA) as gradient ion for loading.

2.1.1. Physicochemical Characterization of LB-MSNs

Size measurements by DLS technique revealed that the particle size of LB-MSNs was 97.33 ± 5.63 nm, upon loading of PA, the size was slightly increased to 110 ± 8.85 nm. No significant change in size was observed before and after drug loading of

MET and TPT with in situ HIP approach (MP)LB-MSNs, (TP) LB-MSNs, and coloaded MSNs, (MP+TP)LB-MSNs. This is again confirmed by the transmission electron microscopy which reveals a uniform intact coating of the lipid bilayer (**Figure 2**A).

Zeta potential measurements of plain MSNs, LB-MSNs, (MP) LB-MSNs, (TP)LB-MSNs, and coloaded (MP+TP)LB-MSNs were shown in Figure 2A. There is a marked difference in zeta potential observed in plain and LB-MSNs which is an indirect confirmation of the intact coating of the lipid bilayer. Drug loading procedures did not affect the zeta potential of the formulations.

To confirm the in situ HIP formation after drug loading, MSNs were evaluated by infrared spectroscopy (Figure 2B). The characteristic peaks at 3466 (O−H stretch), 3166 (N−H stretch), 2927 (N−H stretch), 1640 (C=O stretch), 1507 (C=O stretch), and 1269 cm^{-1} of MET-PA salt were also observed on (MP)LB-MSNs and (MP+TP)LB-MSNs, confirming the formation of HIP inside MSNs. Similarly TPT-PA characteristic peaks 3402 (O−H stretch), 2978 (C−H stretch), 2879 (C−H stretch), 1740 (C=O stretch), 1651 (C=N aromatic stretch), 1590 (C=C aromatic bend), 1506 (C=O stretch), and 1160 cm^{-1} (C−N stretch) were observed in (TP)LB-MSNs and (MP+TP)LB-MSNs. As can be seen clearly, Fourier-transform infrared (FT-IR) spectra of MSNs with PA salts of both MET and TPT closely match with the respective salts (MET-PA and TPT-PA). This confirms the in situ HIP formation between active pharmaceutical ingredient (API) and counterion similar to that of solid salts.

2.1.2. Evaluation of Key Drug Loading Parameters of the Counterion on Drug Loading Efficiency

As a part of the study, we have also evaluated basic parameters such as the type of gradient ion, pH, and temperature that could affect the drug loading efficiency. We have evaluated three gradient ions of PA, sodium, ammonium, and TEA. All the gradient ion concentrations were kept constant at 10×10^{-3} M equimolar concentration of PA throughout the experiment. From the results, it was evident that TEA (42 wt%) was most efficient gradient ion followed by ammonia (32 wt%) and sodium ions (28 wt%) Figure 2C. Apart from this, pH of the outer phase is a critical parameter which affects the gradient required for the influx of drug into MSNs. Both the drugs behaved in a different manner with the pH, since MET is highly ionic in nature, we expected low drug loading into MSNs, but conversely, we observed a better drug loading of MET than TPT, increase in the pH resulting in a slight improvement in loading.

We also considered temperature and duration of incubation on the drug loading. The temperature was found to have a profound effect on drug loading capability for both the drugs. A temperature of 55–60 °C was found to be suitable with an optimum 4 h of incubation time for efficient drug loading (Figure 2C). Increase in drug loading may be due to increased lipid bilayer permeability and higher pore volume at higher temperatures.

2.1.3. In Vitro Drug Release Studies

To evaluate the efficiency of the developed formulation, in vitro drug release studies were performed for (MP)LB-MSNs,
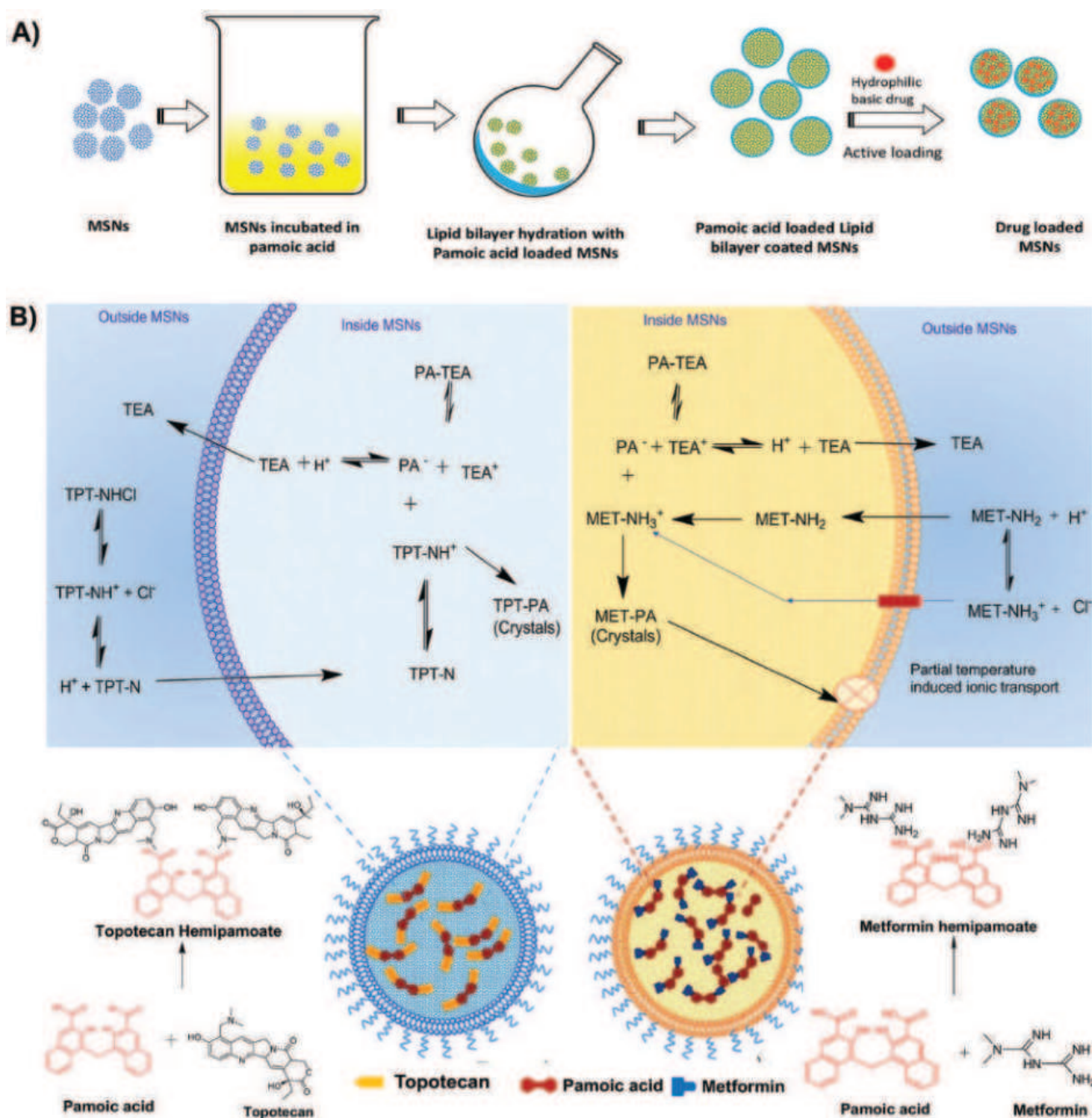
ADVANCED
SCIENCE NEWS
www.advancedsciencenews.com

ADVANCED
HEALTHCARE
MATERIALS
www.advhealthmat.de

Figure 1. A) Schematics depicting the stepwise preparation of LB-MSNs. B) Mechanistic representation of active loading procedure in PA-loaded LB-MSNs, TEA salt of PA present inside the LB-MSNs allows basic drugs into the MSNs due to gradient difference across the membrane. In case of MET, the higher temperatures partially influence the lipid bilayer permeability. Basic drug after reaching inside MSNs reacts with PA and forms a hydrophobic ion pair (HIP) inside MSN.

(TP)LB-MSNs, and coloaded MSNs with and without trapping agent at two different pH 7.4 and 5.5 to simulate blood and tumor microenvironment, respectively. (MP)LB-MSNs showed sustained release up to 48 h with a cumulative drug release of 95% at pH 5.5 and 86.5% at pH 7.4 (Figure 2D). However, drug release from (TP)LB-MSNs was slower than (MP)LB-MSNs, where 76% and 52% of cumulative TPT release was observed at pH 5.5 and 7.4 within 48 h (Figure 2D). No significant

difference in release was observed in the coloaded formulation (MP+TP)LB-MSNs compared to individual drug-loaded formulations. The differential release of MET and TPT from the formulation with trapping agent may be attributed to the difference in hydrophobicities of in situ formed HIPs, MET-PA and TPT-PA, where the solubility of MET-PA (7.4 mg mL^{-1}) was relatively more compared to TPT-PA (0.16 mg mL^{-1}). It was also observed that coloaded formulation without trapping

**ADVANCED
SCIENCE NEWS**

www.advancedsciencenews.com

**ADVANCED
HEALTHCARE
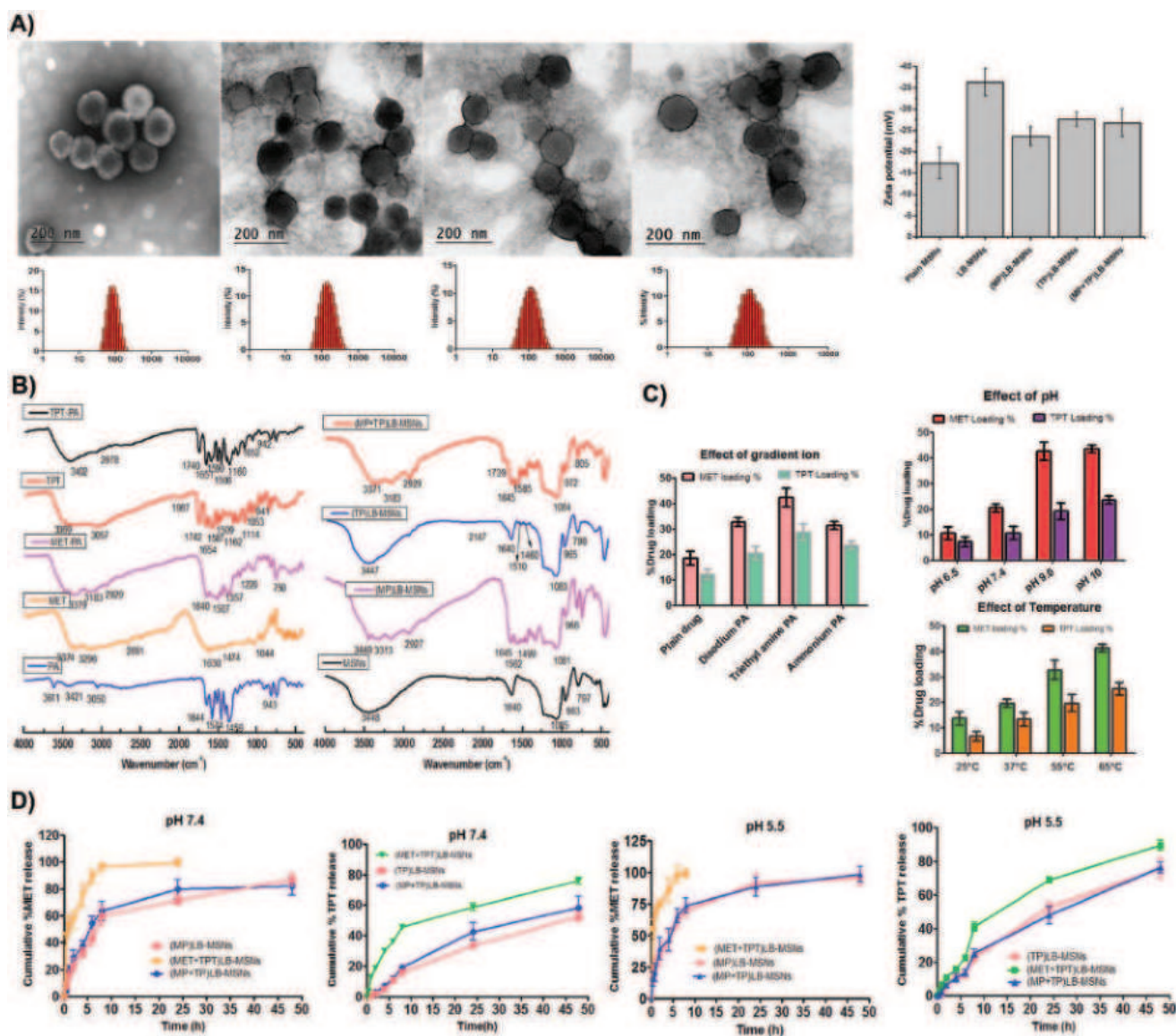MATERIALS**

www.advhealthmat.de

Figure 2. A) Size and polydispersity index (PDI) data of different MSNs, images of transmission electron microscopy (TEM) and dynamic light scattering (DLS) of LB-MSNs, (MP)LB-MSNs, (TP)LB-MSNs, (MP+TP)LB-MSNs (from left to right), and change in zeta potential of different formulations. B) FT-IR of single components (MET, TPT, PA), MET-PA, TPT-PA salts, blank MSNs, and MSNs containing MET, TPT, and PA. C) Various factors affecting the drug loading efficiency; effect of pH, effect of type of gradient ion, and effect of temperature. D) In vitro cumulative percent drug release profiles of MET and TPT from various MSN formulations at pH 7.4 and pH 5.5. All data are expressed as mean ± SD (n = 3).

agent, (MET+TPT)LB-MSN was unable to control the release of MET from the MSNs (75% drug release in 4 h at pH 7.4). But, TPT release was comparatively controlled from MSNs without trapping agent (36.6% in 6 h at pH 7.4) which may be due to inherent lipophilic interactions toward silanol groups of MSNs.

The use of LB-MSNs as a delivery vehicle and in situ HIP formation substantially increase the release time of MET which is a major challenge. Using LB-MSNs, Liu et al. reported irinotecan delivery, in which fivefold increase tumor distribution and 11-fold increase in plasma half-life with a controlled in vivo release of more than 48 h were achieved.[25] Similarly, Meng et al. successfully codelivered gemcitabine and paclitaxel in synergistic ratios using lipid bilayer–coated MSNs with a

controlled release of water soluble gemcitabine for more than 48 h, in vitro.[26] In comparison to similar delivery systems, present results substantiate its efficacy as a codelivery platform to achieve synergistic tumor site concentrations.

2.2. In Vitro Cell Culture Studies

2.2.1. Identification of Effective Synergy Combinations between MET and TPT Using Mathematical Modeling

To evaluate the combined effects of MET and TPT, 6 × 6 concentration combination experiments were performed in

ADVANCED
SCIENCE NEWS
www.advancedsciencenews.com

ADVANCED
HEALTHCARE
MATERIALS
www.advhealthmat.de

MDA-MB-231 and 4T1 cell lines using 3-(4,5-dimethylthiazol-2-yl)-2,5-diphenyltetrazolium bromide (MTT) assay after 48 h treatment. We have investigated concentration ranges, $0.01 \times 10^{-3} - 5 \times 10^{-3}$ M of MET and $0.01 \times 10^{-6} - 5 \times 10^{-6}$ M of TPT. After MTT treatment and obtaining the growth inhibition data, we have used COMBENFIT software package to objectively identify the synergistic combinations of MET and TPT. We assessed the region of the synergy of each combination independently with three established mathematical models, such as Bliss, Loewe, and highest single agent (HSA) models.[27] Particulars of these models and their relative advantages can be found in previous publications.[28] From the modeling data, we identified that effective synergy was present with $0.05 \times 10^{-3} - 0.5 \times 10^{-3}$ M of MET and $0.1 \times 10^{-6} - 1 \times 10^{-6}$ M of TPT in both the cell lines (**Figure 3**A and Figure S4A (Supporting Information)). The analysis of single-agent effect reveals, that inhibitory concentration (IC50) (IC50) of MET and TPT was 3.95×10^{-3} M and 1.15×10^{-6} M, respectively, in MDA-MB-231 cell line and 3.59×10^{-3} M and 1.01×10^{-6} M in 4T1 cell line, respectively (Figure 3C and Figure S4C (Supporting Information)).

After identification of the synergy combinations, we tried to analyze the same with the developed formulations. We
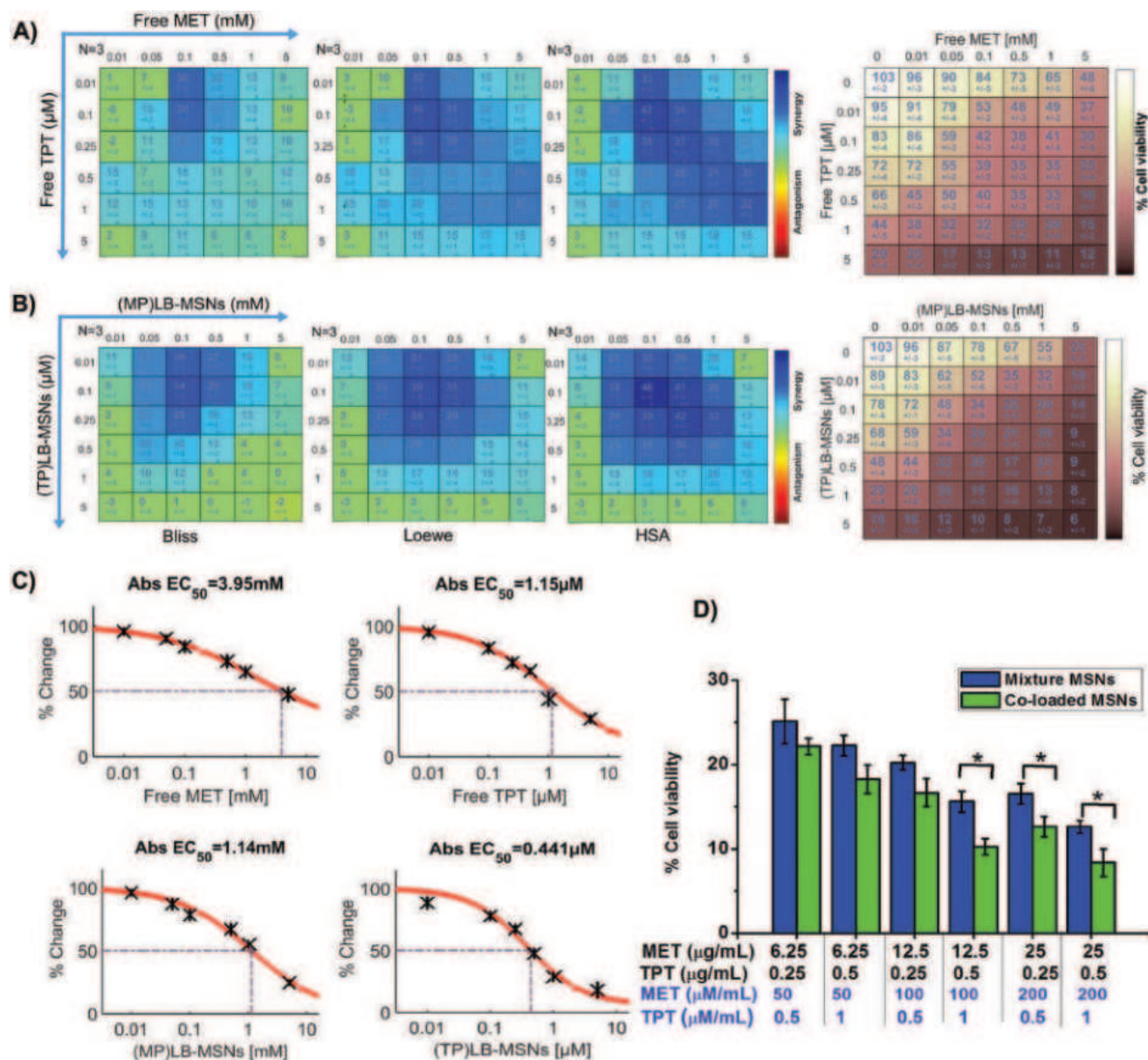

Figure 3. Predicted inhibition data of the three synergy models [Bliss, Loewe, highest single agent (HSA)] in MDA-MB-231 cells treated with A) free MET (x-axis) and free TPT (y-axis), B) (MP)LB-MSNs and (x-axis) and (TP)LB-MSNs (y-axis) in 6 × 6 concentration checkerboard format for 48 h using MTT assay. All data are expressed as mean ± SD, n = 3, *p ≤ 0.05; **p ≤ 0.01; the synergy spots are represented blue in the matrix and experimental data of growth inhibition compared with control are presented. C) Single-agent effect IC50 of the individual drug and drug-loaded LB-MSNs. D) Comparative growth inhibition data of the coloaded and mixture formulations in definite ratios. All data are expressed as mean ± SD, n = 3, *p ≤ 0.05.

repeated the same experiment with a mixture of individual drug-loaded LB-MSNs, i.e., (MP)LB-MSNs and (TP)LB-MSNs in the drug equivalent ratios. After data treatment, we found a good enhancement in the representative synergistic score of the individual models with a significant reduction in the individual IC50 values (Figure 3B and Figure S4B (Supporting Information)). It was found that IC50 of (MP)LB-MSNs and (TP)LB-MSNs was reduced to 1.14×10^{-3} and 0.44×10^{-6} M, 1.33×10^{-3} and 0.40×10^{-6} M in MDA-MB-231 and 4T1 cell lines, respectively (Figure 3C and Figure S4C (Supporting Information)). IC50 of encapsulated drugs were 35–50% lower than free drugs. From the data, it was also clear that synergy was present with 0.05×10^{-3}–1×10^{-3} M of MET and 0.1×10^{-6}–1×10^{-6} M of TPT.

To observe the cytotoxicity of the drug-free MSNs, we carried out the cell viability studies for blank LB-MSNs and (PA) LB-MSNs up to 5 mg mL^{-1} concentration in MDA-MB-231 and 4T1 cell lines. From the results (Figure S3, Supporting Information), it was clear that drug-free LB-MSNs and pamoic acid-loaded LB-MSNs, and (PA)LB-MSNs did not exert cytotoxic effects at the experimental concentrations of in vitro studies.

Based on these modeling data, practical formulation, and dosing aspects, we tried to rationally design the coloaded LB-MSNs. Initially, we have selected six combinations of MET/TPT (50/0.5, 50/1, 100/0.5, 100/1, 200/0.5, and 200/1 of MET/TPT ($\times 10^{-6}$ M)). From the MTT assay, it was observed that coloaded formulations were proven furthermore efficacious compared to a mixture of individual formulations (Figure 3D). Considering the practical loading aspects in MSNs and clinically relevant dosing, we have selected 200/1 (in $\times 10^{-6}$ M) molar ratio of MET/TPT for in vivo studies which meets the practical loading of 25 (wt%) MET and 0.5 (wt%) TPT loading.

2.2.2. Cell Uptake Studies

To evaluate the codelivery efficiency of the LB-MSNs, cellular uptake behavior was monitored in MDA-MB-231 cells using confocal microscopy. To test the hypothesis that the coloaded nanoparticles ensure the deterministic delivery of both cytotoxic drugs versus stochastic distribution in a mixture of nanoparticles, we engineered nanoparticles tagged with fluorescein isothiocyanate (FITC) (green) or rhodamine B, (Red) tracers. MDA-MB-231 cells were incubated with either a combination of FITC-loaded LB-MSNs, (FITC)LB-MSNs, and rhodamine B-loaded LB-MSNs, (RhB)LB-MSNs, or coloaded MSNs, (FITC+RhB)LB-MSNs which contain both the tracers. Interestingly, confocal microscopy revealed that while a large fraction of cells internalizes both the nanoparticles, there was certain cell population that took up either FITC or RhB particles alone (Figure S5, Supporting Information).

2.2.3. Codelivery of MET and TPT Enhances Induction of Cell Cycle Arrest and Apoptosis via Alteration in Mitochondrial Membrane Potential

To further evaluate the intracellular effects of various formulations loaded with MET and TPT alone and in combination, cell cycle analysis, mitochondrial membrane potential, and apoptosis studies were performed using flow cytometric analysis. In cell cycle analysis, the nuclear content of the treated cells was quantified on the basis of propidium iodide (PI) signals and mitochondrial membrane depolarization was measured with the help of JC-1 dye. To quantify the apoptosis, widely used Annexin-V FITC binding–based flow cytometric assay was performed. It is well known that apoptosis occurs by two pathways: the death receptor–mediated and mitochondrial pathways.[29] It is widely studied that mitochondrial depolarization is one of the major pathway involved in the apoptosis induced by MET[30] and TPT.[31] As illustrated in **Figure 4**, the treatment with MET and TPT alone and in combination induced mitochondrial membrane depolarization that leads to cell cycle arrest and subsequently apoptosis. MSNs loaded with MET and TPT, [(MP)LB-MSNs, (TP)LB-MSNs, and (MP+TP)LB-MSNs)] further enhanced the apoptotic effects via mitochondrial membrane depolarization in a synergistic manner. Quantitatively, free MET and TPT induce mitochondrial depolarization in 14.03% and 15.01% cell population, respectively. But, in combination treatment with free drugs slightly enhanced the population which was observed to be antagonistic. Drug-loaded LB-MSNs significantly enhanced the depolarization representing 27.08% and 31.03% of cell population for (MP)LB-MSNs and (TP)LB-MSNs, respectively. In combination treatment, coloaded formulation, (MP+TP)LB-MSNs had shown higher depolarization (54.98%) compared to mixture LB-MSNs (42.25%) and Free MET+TPT (20.81%).

As depicted from the cell cycle analysis data, free MET and (MP)LB-MSNs displayed vivid G1 phase arrest via activation of AMPK through upregulation of p53–p21^{waf1} axis.[32] Whereas free TPT, (TP)LB-MSNs showed prominent G2 phase arrest. Compared to plain TPT (G2-21.89%) (TP)LB-MSNs induced more G2 phase arrest. In combination studies, the effect of MET+TPT showed a pronounced effect compared to individual treatments and it was also observed that MET+TPT combination induced more S phase and G2 phase arrest contrary to G1 phase arrest. Quantitatively, there was more pronounced effects observed in groups of the coloaded formulation (MP+TP) LB-MSNs, (G2-39.84%, S-57.72%), compared to the mixture of drug loaded MSNs (MP)LB-MSNs+(TP)LB-MSNs, (G2-41.5% S-47.46%). In a similar manner subsequent to cell cycle arrest, treatment with coloaded formulation induced more apoptosis compared to the mixture of MSNs loaded with two individual drugs after 48 h of treatment. (MP+TP)LB-MSNs induced 65.52% of apoptosis compared to a mixture of MSNs loaded with individual drugs, 47.94%. This represents that the codelivery of MET and TPT demonstrated collaborative effects on mitochondrial depolarization and cell cycle arrest, resulting in MDA-MB-231 cell apoptosis. This clearly demonstrates that the deterministic delivery of drugs in a single nanoparticle system would be more advantageous compared to a mixture of nanoparticles.

2.3. In Vivo Studies

2.3.1. In Vivo Near Infrared Fluorophore (NIRF) Live Imaging

In order to follow the biodistribution of the LB-MSNs to the tumor site, animals were intravenous (i.v.) injected with
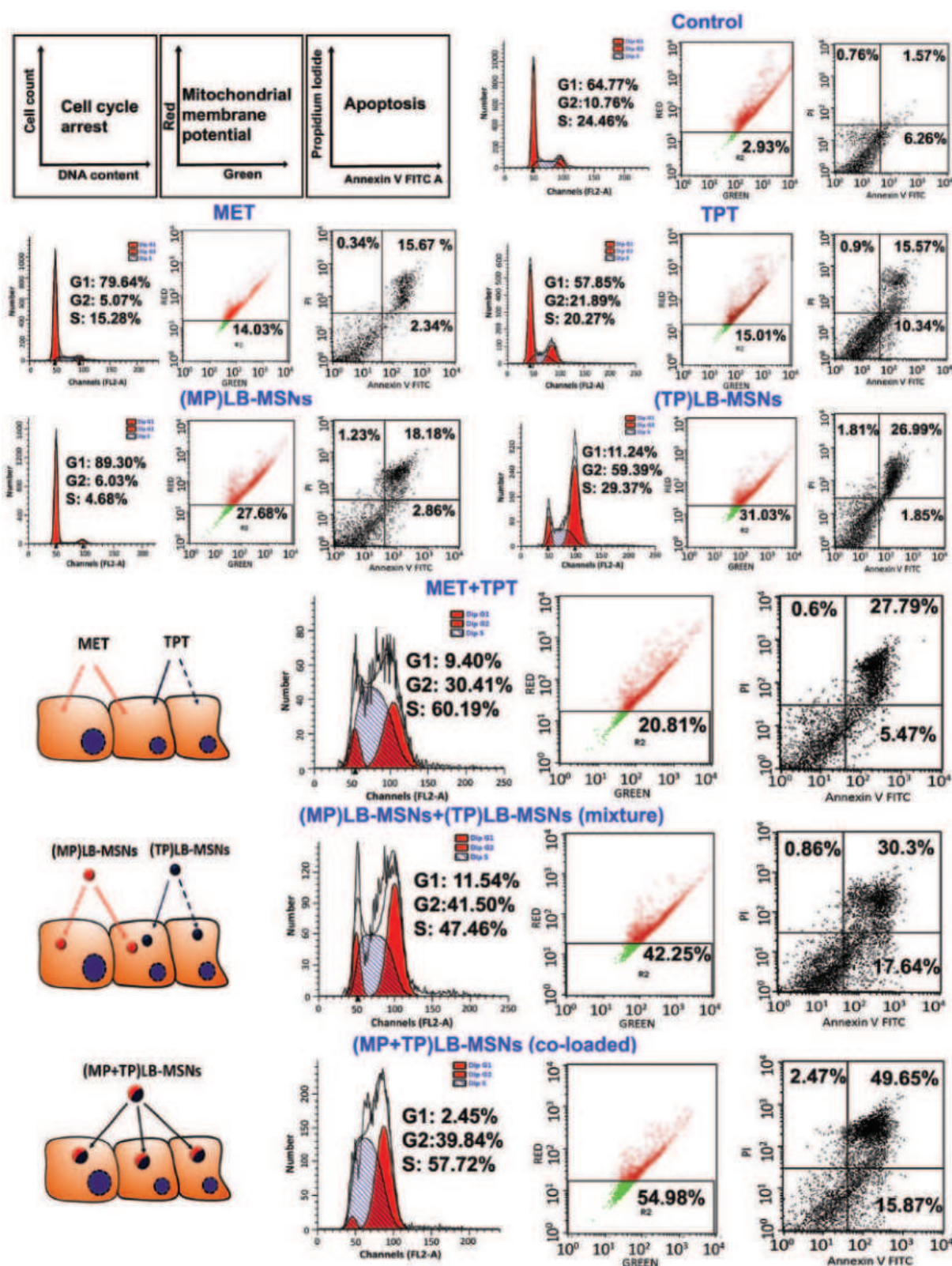
Figure 4. Representative flow cytometry images of cell cycle arrest, mitochondrial membrane potential, and apoptosis showing the combined effect of free MET+TPT and various LB-MSN formulations in MDA-MB-231 cell lines. Cell cycle arrest and mitochondrial membrane potential were performed after 24 h treatment and apoptosis was performed at 48 h with free drugs (MET and TPT) and LB-MSN formulations alone and in combinations. In combination experiments, 200×10^{-6} M of MET and 1×10^{-6} M TPT were used. All results were obtained in triplicate ($n = 3$).

near-infrared (NIR)-labeled (DiR740)LB-MSNs, after achieving the 200–300 mm³ tumor size (**Figure 5**A). IVIS imaging was obtained prior to and following IV injection of 1 mg kg⁻¹ equivalent, DiR-labeled LB-MSNs at the designated time points. Robust fluorescence intensity was observed at the tumor sites within 4 h of LB-MSN injection, following which the signal was sustained for at least 24 h. This was also confirmed by ex vivo imaging of the tumors and major organs collected from the animals, following sacrifice 24 h postinjection (Figure 5A1,A2). In addition to abundant particle uptake at the tumor site, the

liver and spleen were also major sites of particle distribution. Little signaling was obtained in the lung and kidney.

2.3.2. Pharmacokinetics and Tumor Distribution

To determine the effect of HIP on pharmacokinetics and tumor distribution of MET and TPT, we have compared coloaded particles with and without trapping agent after i.v. administration. Tumor-bearing mice were injected with MET+TPT
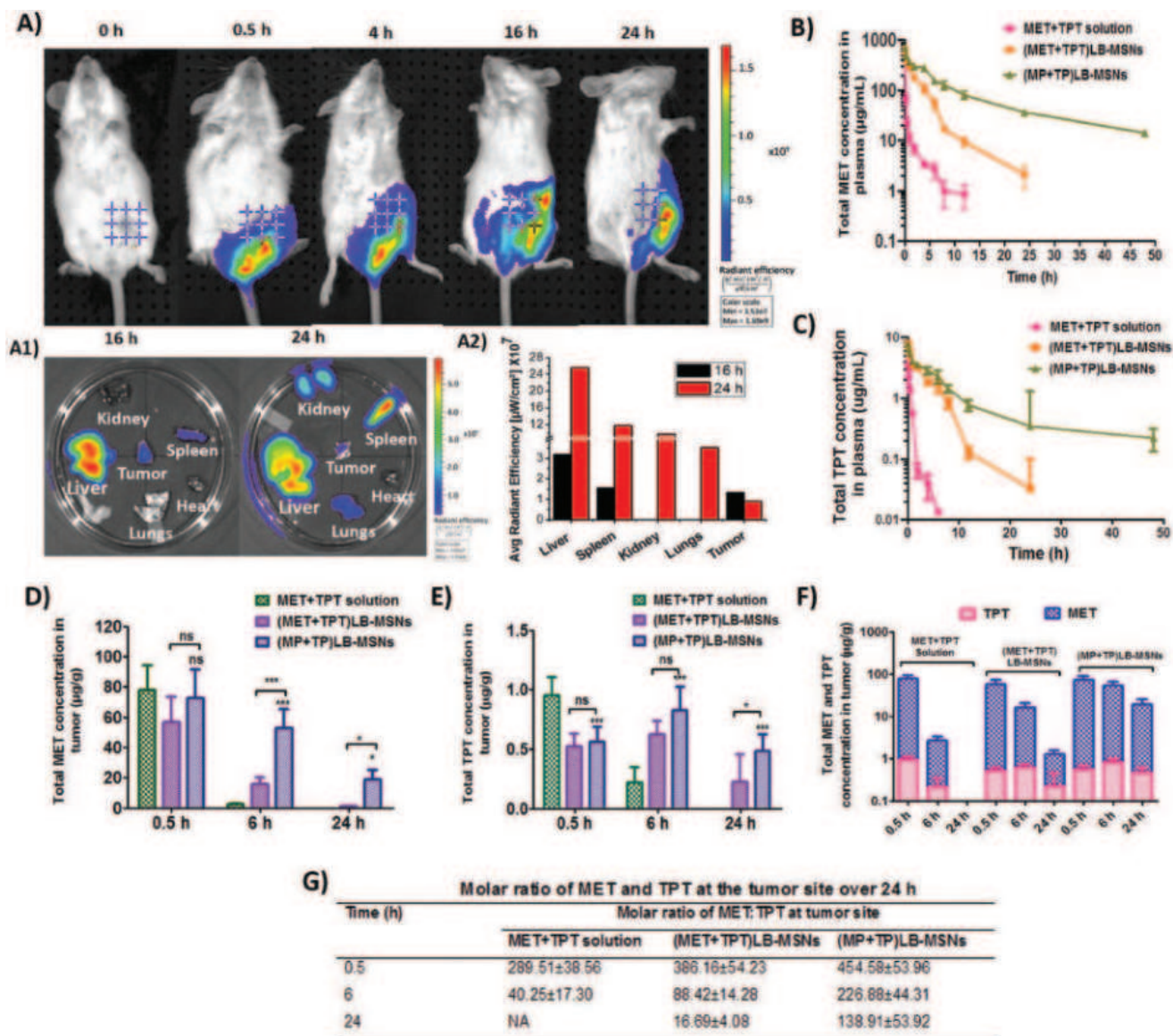

Figure 5. A) Representative IVIS images over 24 h to compare the biodistribution of i.v. injected DiR-labeled LB-MSNs to the 4T1 tumor-bearing mice and A1) ex vivo biodistribution of explanted organs in the same experiment; animals were sacrificed after 16 h and 24 h. A2) Comparative radiant efficiency in different organs of interest. B,C) MET and TPT concentrations in plasma of different coloaded LB-MSNs with and without trapping agent (MET and TPT were given a dose of 50 and 1 mg kg⁻¹, respectively). D) Total MET concentration, E) total TPT concentration in tumor tissue with respect to time, all data are expressed as mean ± SD ($n = 3$), statistical significance was determined with one-way ANOVA and differences between groups were determined by Tukey's multiple comparison test, *$p \leq 0.05$; **$p \leq 0.01$; ***$p \leq 0.001$; ns, nonsignificant. F) Comparison of total MET and TPT tumor accumulation between the MET+TPT solution and different LB-MSN formulations. G) Molar ratio of MET and TPT at tumor site as free or LB-MSN formulations.

Table 1. Pharmacokinetic parameters of MET and TPT in mice plasma after single intravenous administration of coloaded MET and TPT formulations at a dosage of 50 mg kg^{-1} MET and 1 mg kg^{-1} TPT. Significance level: ***$p \leq 0.001$; **$p \leq 0.01$; *$p \leq 0.05$; ns, nonsignificant versus MET+TPT solution, all data are expressed as mean ± SD ($n = 3$).

	Metformin (MET)			Topotecan (TPT)		
	MET+TPT solution	(MET+TPT)LB-MSNs	(MP+TP)LB-MSNs	MET+TPT solution	(MET+TPT)LB-MSNs	(MP+TP)LB-MSNs
C_{max} [µg mL^{-1}]	542.61 ± 17.84	707 ± 25.45	681.76 ± 134.64	3.60 ± 0.028	7.92 ± 0.073	7.74 ± 0.063
$t_{1/2}$ [h]	3.34 ± 1.37	5.84 ± 1.202^{ns}	14.42 ± 2.58***	1.76 ± 0.028	2.97 ± 0.11***	10.90 ± 0.733***
AUC$_{0-t}$ [µg h mL^{-1}]	694.8 ± 734.63	1355.66 ± 74.24^{ns}	3887.73 ± 340.22***	2.21 ± 0.89	23.120 ± 3.09***	42.063 ± 0.591***
V_{ss} [mL]	155.70 ± 16.5	128.17 ± 14.24	175.59 ± 1.21	6.75 ± 0.19	3.32 ± 0.013	6.25 ± 0.022
Cl [mL h^{-1}]	158.29 ± 3.5	36.33 ± 2.29***	11.99 ± 1.16***	8.88 ± 0.12	0.859 ± 0.0061***	0.430 ± 0.0038***
MRT [h]	1.92 ± 1.79	3.54 ± 0.61^{ns}	14.67 ± 0.87***	0.75 ± 0.04	3.87 ± 0.22***	14.52 ± 0.62***

solution, (MET+TPT)LB-MSNs, and (MP+TP)LB-MSNs through tail vein at an equivalent dose of 50 mg kg^{-1} MET and 1 mg kg^{-1} TPT. Plasma distribution profiles over 48 h are shown in Figure 5B,C, and pharmacokinetic parameters are summarized in **Table 1**. MET+TPT solution eliminated rapidly from the systemic circulation, whereas coloaded MSNs with trapping agent, (MP+TP)LB-MSNs exhibited 2.8-fold, 5.6-fold increase in area under curve (AUC)$_{0-\alpha}$ of MET and 1.8-fold and 19-fold increase in AUC$_{0-\alpha}$ of TPT compared to (MET+TPT)LB-MSNs and MET+TPT solution, respectively. The average half-life of (MP+TP)LB-MSNs was 2.4-fold and 4.3-fold longer for MET and 3.6-fold and 6.7-fold longer for TPT compared to the formulation without trapping agent and drug solutions, respectively. These results indicate longer residence of drug in the body by HIP-based coloaded MSNs which further helps in promoting tumor site accumulation by enhanced permeation and retention (EPR) effect. The lower mean residence time (MRT) and half-life of the MET+TPT solution might be attributed to the rapid distribution of the free drug to organs and rapid elimination. Further, a significant difference between the pharmacokinetic parameters of (MP+TP)LB-MSNs and (MET+TPT)LB-MSNs might be due to the faster release of drugs from the MSNs without trapping agent. Increased AUC$_{0-\alpha}$, MRT, and $t_{1/2}$ values of (MP+TP)MSNs claim the controlled release effect of HIP and long circulation due to lipid bilayer coating.

A comparative tumor distribution study was also performed to assess the tumor localization of the formulations. Figure 5D,E compares the MET and TPT concentrations in the tumor at a different time resulting due to various formulations. Apparently, (MP+TP)LB-MSNs delivered more MET and TPT than MET+TPT solution and (MET+TPT)LB-MSNs. To prove the in vivo synergistic efficacy, it is always necessary to deliver the drug ratios exhibiting synergistic cytotoxicity.[15c] To confirm the delivery of synergistic ratio, we have determined the MET:TPT ratio at the tumor site (Figure 5F). The coloaded formulation with trapping agent, (MP+TP)LB-MSNs had maintained molar ratios of MET to TPT at 138.9 to 454.5 at the end of 24 h, which absolutely fall under the region of synergy determined in in vitro synergy modeling experiments. In contrast, MET+TPT solution reached the tumor at synergistic molar ratios in early time points with no detectable limits at 24 h. Further comparison between formulations with and without trapping agent showed low molar ratios of MET to TPT

from (MET+TPT)LB-MSNs, ranging from 16 to 386, clearly demonstrating that HIP-based controlled release of MET and TPT helps in maintaining high tumor site concentrations for a prolonged period of time (Figure 5G).

2.3.3. In Vivo Tumor Regression Studies

After having superior in vitro activity and improved pharmacokinetics, various LB-MSNs were tested for in vivo efficacy in BALB/c mice bearing 4T1 mammary tumors and compared with free MET, TPT, and control. Treatment was started when the tumor volume reached ≈100 mm^3 in all the animals. Each group received i.v. dose of MET and TPT equivalent to 50 and 1 mg kg^{-1}, respectively, on days 1, 4, 8, 12, and 16. The tumor volume versus time curve and tumor photographs are presented in **Figure 6**A,D. Tumor volume was measured throughout the study, and animals were sacrificed on the 20th day of the study started, to harvest the tumors and organs. As shown in Figure 6A, for single drug formulations, both (MP)LB-MSNs and (TP)LB-MSNs had slightly better antitumor activity than the corresponding drug solutions, but no significant difference was observed ($p > 0.05$). For combination formulations, the tumor growth was better inhibited than single drug-loaded formulations. The mixture of solutions (MET+TPT solution) and a mixture of single drug loaded MSNs (MP)LB-MSNs+(TP)LB-MSNs had similar effects. Coloaded (MP+TP)LB-MSNs showed superior antitumor activity than their solutions and the mixture of single drug loaded LB-MSNs with significant differences ($p \leq 0.05$). The final tumor volume at the end of 20 days post-treatment of coloaded (MP+TP)LB-MSNs treated group was 13.9-fold, 4.06-fold, and 1.84-fold lower than control, free MET+TPT, and mixture (MP)LB-MSN+(TP)LB-MSN-treated groups, respectively. Whereas, mixture of LB-MSNs had shown 7.5-fold and 2.20-fold lower tumor volumes compared to control and free MET+TPT groups, respectively. The final tumor weight of coloaded formulation at the end of tumor regression study was 32-fold, 9.69-fold, and 2.29-fold lower than the control group, MET+TPT solution, and mixture(MP)LB-MSN+(TP)LB-MSN group ($p < 0.001$) (Figure 6B). The body weight of mice was also recorded to evaluate the safety of the formulations. As seen in Figure 6C, TPT solution and (TP)LB-MSNs showed
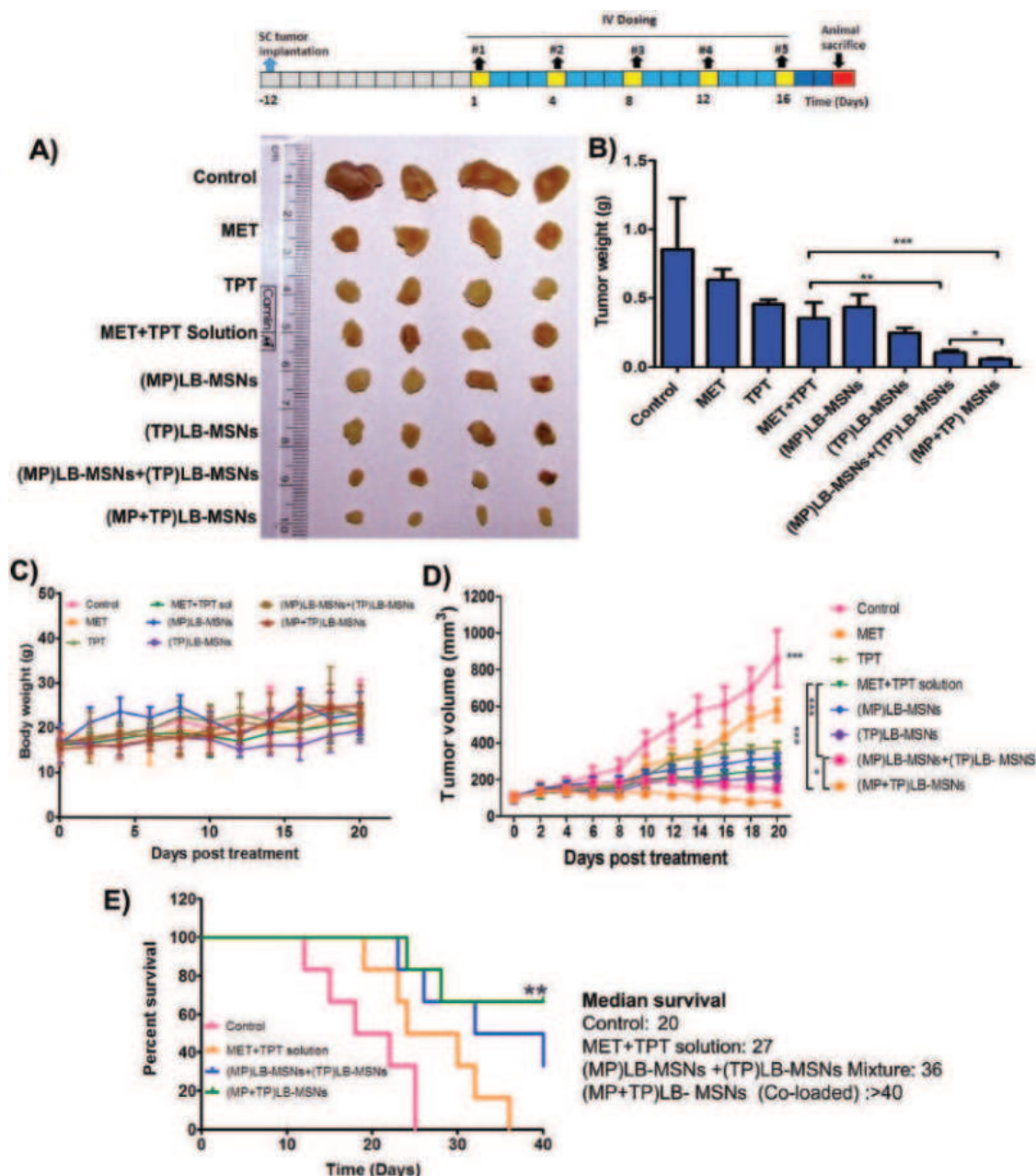
Figure 6. In vivo antitumor activity against 4T1 cells transplanted mammary tumor in female BALB/c mice (MET dose: 50 mg kg^{-1} and TPT dose: 1 mg kg^{-1} body weight). A) Morphology of the tumors harvested at the end of the study. B) Tumor volume versus time at different time points of the study. All data are expressed as mean ± SD ($n = 6$), statistical significance was determined with one-way ANOVA analysis. Differences between groups were determined by a Tukey's multiple comparison test, *$p \leq 0.05$; **$p \leq 0.01$; ***$p \leq 0.001$; ns, nonsignificant. C) Body weight changes during the study period. D) Survival rates of 4T1 tumor-bearing mice administrated with a MET+TPT solution and MET+TPT-loaded LB-MSNs, survival data were generated by the Kaplan–Meier method, median survival and statistical significance were determined by log-rank test and Mann–Whitney U test, respectively ($n = 6$), **$p \leq 0.01$.

comparative weight loss than free MET and its combination treatment arms MET+TPT solution, (MP)LB-MSNs+(TP)LB-MSNs, and coloaded (MP+TP)LB-MSNs, indicating that MET increasing the safety profile of the TPT. The better tumor inhibition efficacy of coloaded formulations can be attributed to better pharmacokinetic profile and controlled drug delivery with the ratiometric synergistic combinatorial delivery of MET and TPT which resulted in higher residence

time in body compared to free drug solution that was getting rapidly eliminating from the body.

2.3.4. Survival Analysis

The survival studies were performed for 40 days after the treatment started, and it was found that survival rates

**ADVANCED
SCIENCE NEWS**
www.advancedsciencenews.com

**ADVANCED
HEALTHCARE
MATERIALS**
www.advhealthmat.de

increased significantly on the administration of coloaded LB-MSNs in comparison to the MET+TPT solution and mixture LB-MSNs. The median survival times for mice treated with saline, MET+TPT solution, mixture of (MP)LB-MSNs+(TP) LB-MSNs, and coloaded (MP+TP)LB-MSNs were 20, 27, 36, and >40 days, respectively (Figure 6E). Treatment with MET+TPT solution and mixture LB-MSNs showed slightly improved survival profiles, whereas coloaded (MP+TP)LB-MSNs enhanced median survival time more than 40 days ($p \leq 0.01$).

3. Conclusion

In this study, we successfully developed a novel in situ HIP-based active loading technique for the efficient loading and controlled release of MET and TPT using pseudo-cell-like LB-MSNs as templates. The developed delivery system was able to control the release of MET and TPT. This resulted in significantly increased intracellular concentrations of MET which is a major translational concern in the MET therapy in cancer. By rational design of these LB-coated MSNs with the synergistic ratio of intended drugs identified by synergy modeling provides deterministic delivery of drug inside the tumor cells. Co-loaded MET and TPT formulations demonstrated higher in vitro cytotoxicity and related apoptotic effects compared to the mixture of single drugs and drug-loaded MSNs. The enhanced tumor efficacy was consistent with the in vitro cell cycle and apoptotic effects. All these presented results prove that translational challenges of MET could be successfully addressed by rational design of the high payload bearing MSNs with controlled release profile. Since the safety and clinical benefits are already proven with other chemotherapeutic agents, therapies could be designed by appropriate selection and delivery of the synergistic ratios at the tumor site. To the best of our knowledge, the present reported active loading procedure using LB-MSNs is the first of its kind and this could be a novel platform technology for the ionic drugs which are difficult to load by using conventional active loading techniques.

4. Experimental Section

Materials: MET was procured from Sigma-Aldrich (St. Louis, MO, USA), TPT HCl was received as a gift sample from Dabur Pharmaceuticals Pvt. Ltd. DSPE-PEG$_{2000}$, soya phosphatidylcholine, cholesterol, cetyltrimethylammonium bromide (CTAB), Pluronic F-127 were purchased from Sigma-Aldrich (St. Louis, MO, USA). Tetraethylorthosilicate (TEOS), and pamoic acid disodium salt were purchased from TCI chemicals, India Pvt. Ltd. Cell culture media and supplements were purchased from Invitrogen (Carlsbad, CA). MTT, FITC, PI, and RNase were purchased from Sigma-Aldrich (St Louis, MO, USA). High performance liquid chromatography (HPLC) solvents such as acetonitrile and methanol were purchased from Merck (India). All other chemical reagents were of analytical, cell culture grade and obtained from commercial sources. Triple-distilled water (TDW) was prepared from Milli Q system (Millipore, Bedford, MA, USA).

Identification of Synergy between MET and TPT: Before formulation development, the synergy between MET and TPT was screened by using regular cytotoxicity assay (MTT assay). To identify the synergy

combinations, 6×6 checkerboard format was used, and results were evaluated using COMBENEFIT software package. The detailed procedure of MTT assay and modeling is discussed in cell culture section provided in the Supporting Information.

Selection of APIs and Counterion for HIP Formation: Based on the acid dissociation constants (pK_a) of MET, 12.4, and TPT, 8 and 9.83, PA was evaluated as the counterion for the HIP formation. The detailed procedure of HIP synthesis and evaluation is provided in the Supporting Information.

Preparation of LB-MSNs and Drug Loading by Using the HIP Approach—Loading of Pamoic Acid into MSNs and Lipid Bilayer Coating (PA)LB MSNs: Typical MSN cores were prepared by well-reported Stöbers process[33] (see the Supporting Information for detailed procedure). PA-loaded MSN cores were prepared by passive adsorption process. Briefly, 100 mg of plain MSNs were soaked in 5 mL of aqueous 10×10^{-3} M solution of PA (disodium salt) followed by probe sonication for 2 min with a power output of 20 W. After sonication, MSN suspension was incubated in the same solution for 12 h. The PA-loaded particles were then coated with a lipid film obtained by solvent evaporation of a mixture of 25 mg of SoyPC/Chol/DSPE-PEG$_{2000}$ (molar ratio 7:2.75:0.25) dissolved in chloroform to a 25 mL round bottom flask under rotary evaporation. For uniform coating of the lipid film, probe sonication was used for 10 min with intermittent on/off cycles at a power output of 25 W. Unentrapped PA was removed by centrifugation at 12 000 rpm for 15 min.

Preparation of LB-MSNs and Drug Loading by Using the HIP Approach—Use of (PA)LB MSNs for Remote Loading of MET and TPT: Different conditions were used for the active loading of MET and TPT. MET at a concentration of 10 mg mL^{-1} was dissolved in phosphate buffered sucrose (10% w/v sucrose and phosphate buffered saline (PBS) pH 9), which was mixed with (PA)LB-MSNs to achieve a MET/MSN weight ratio of 1:1. Similarly, TPT at 1 mg mL^{-1} was dissolved in PBS and was mixed with (PA)LB-MSNs to achieve TPT/MSN ratio of 1:2. After that, the mixture was incubated for 4 h at 60 °C under constant shaking. Similar conditions were followed for coloading of both MET and TPT. The ratio of MET and TPT was adjusted based on the percent of entrapment of individual drugs. After incubation, drug-loaded particles were centrifuged at 10 000 rpm for 15 min, and the supernatant was removed and replaced with 10% sucrose for the lyophilization. Lyophilization was carried out at −55 °C for 24 h under 0.1 bar vacuum. For comparative evaluation, formulations without trapping agent were prepared using passive adsorption process and the rest of the procedure was same.

Preparation of LB-MSNs and Drug Loading by Using the HIP Approach—Physicochemical Characterization of LB-MSNs: All developed formulations were evaluated for particle size, zeta potential, drug loading efficiency, in vitro drug release profiles, and confirmation of in situ HIP formation. Apart from that, various parameters that affect the drug loading conditions like, pH, type of gradient ion, and temperature were also evaluated. To confirm the membrane permeability of metformin, in vitro permeability assay was also performed. Detailed methods are described in the Supporting Information.

Preparation of LB-MSNs and Drug Loading by Using the HIP Approach—In Vitro Cell-Based Assays: To evaluate the efficiency of developed formulation, cell-based assays were performed in MDA-MB-231 and 4T1 (human and mouse, respectively) breast cancer cell lines by following established experimental protocols. Cytotoxicity assays and synergy calculations were performed by modeling approach using COMBENEFIT software package in 6×6 checkerboard format. Other cell-based assays like cell cycle arrest, apoptosis, mitochondrial membrane potential, cell uptake studies were performed as per the manufacturer and reported experimental protocols. A detailed description of experimental procedures and conditions is provided in the Supporting Information.

Preparation of LB-MSNs and Drug Loading by Using the HIP Approach—In Vivo Studies: All the animals for in vivo experiments were procured from the National Laboratory Animal Center (NLAC) CDRI and acclimatized for 1 week. All the protocols for animal experiments were

approved by the Institutional Animal Ethical Committee CSIR–CDRI (approval no: IAEC/2016/159).

Preparation of LB-MSNs and Drug Loading by Using the HIP Approach—Tumor Model Development: Subcutaneous murine breast cancer model was used for the evaluation of the developed formulations. The breast cancer model was developed in 6–8 week old female BALB/c mice weighing 20–22 g using murine mammary carcinoma cells, 4T1. Cells at a density of 1×10^6 were injected subcutaneously at the mammary gland near to lower right quadrant of the abdomen of mice. In vivo NIRF imaging, pharmacokinetics, and tumor distribution studies were carried out in mice with a tumor volume ranging 200–300 mm³, whereas tumor regression study and survival analysis were performed in mice with 100 mm³ tumor volume.

Preparation of LB-MSNs and Drug Loading by Using the HIP Approach—In Vivo NIRF Imaging: In order to observe the biodistribution of the LB-MSNs intuitively, real-time NIRF imaging was applied to monitor the fate of the LB-MSNs in vivo. DiR, a NIRF dye, was selected as an indicator and MSNs were prepared by passive loading approach similar to the procedure followed for the preparation of dye-loaded MSNs in cell uptake studies. 150 µL of (DiR)LB-MSNs containing DiR dose of 1 mg kg⁻¹ was injected intravenously via tail vein to 4T1 tumor-bearing female BALB/c mice. After 0.5, 4, 16, and 24 h, mice were anesthetized with 2% isoflurane and placed on their back into a light-tight chamber. At the end of the imaging, the mice were sacrificed and heart, liver, spleen, lung, kidney, and tumor were harvested for ex vivo imaging. The real-time NIRF images were taken using Xenogen IVIS Lumina system (Caliper Life Sciences, USA) with the indocyanine green (ICG) filter (excitation at 745 nm, emission at 835 nm) at time points. The exposure time was set to 3 s. Results were analyzed using Living Image 3.1 software (Caliper Life Sciences, USA).

Preparation of LB-MSNs and Drug Loading by Using the HIP Approach—Pharmacokinetics and Tumor Distribution of MET and TPT from Various Formulations: In order to evaluate the in vivo codelivery of MET and TPT MSNs and the effect of ion trapping agent on the release and distribution, 4T1 tumor-bearing female BALB/c mice were used and they were compared with plain drugs. When tumor volume reached 200–300 mm³, mice were assigned into 3 groups, 1) free MET+TPT solution, 2) coloaded (MET+TPT)LB-MSNs, without trapping agent, 3) coloaded (MP+TP)LB-MSNs, with trapping agent containing MET and TPT equivalent to 50 and 1 mg kg⁻¹, respectively. At designated time points, mice were anesthetized, blood was collected, plasma separated by centrifugation, and stored at −20 °C until analysis. Tumors were collected and frozen immediately and stored at −80 °C. After extraction from the biological samples, MET and TPT were analyzed by HPLC method as described and plasma concentration–time profiles were fitted to the noncompartmental analysis using Pheonix software package.

Preparation of LB-MSNs and Drug Loading by Using the HIP Approach—In Vivo Antitumor Efficacy: In vivo antitumor efficacy of the MET- and TPT-loaded MSNs was evaluated in 4T1 cells bearing mouse model. When the tumor size reached ≈100 mm³, mice were randomly divided into eight groups (n = 5) and administered through i.v. route with saline, MET solution, TPT Solution, MET+TPT solution, (MP)LB-MSNs, (TP)LB-MSNs, (MP)LB-MSN+(TP)LB-MSN mixture, and coloaded (MP+TP) MSNs, respectively, through tail vein on days 0, 4, 8, 12, and 16. The dosage of MET or TPT was kept at 50 and 1 mg kg⁻¹, respectively. Tumor volumes were measured throughout the experiment and calculated according to the formula: $(L \times W^2)/2$, in which L is the longest and W is the shortest tumor diameter (mm). Mice were sacrificed, and tumors were harvested at the completion of the experiment. Changes in body weights were also measured regularly as the indicator of general toxicity. After completion of experiment tumors was excised, tumor weights were measured and tissues were collected for histology.[27a]

Preparation of LB-MSNs and Drug Loading by Using the HIP Approach—Survival Analysis: In a separate experiment similar to the tumor regression study, 4T1 tumor-bearing mice were divided into four groups with six animals in each group (control, MET+TPT solution, (MP)LB-MSN+(TP)LB-MSN mixture, and coloaded (MP+TP)LB-MSNs

and treatment was started after reaching the tumor volume 100 mm³. Animals were treated as per the protocol described above in the tumor regression study. However, survival study was conducted up to 40 days after the treatment started and end point of survival was defined as animal death or when implanted tumor volume reaches ≈1000 mm³.

Preparation of LB-MSNs and Drug Loading by Using the HIP Approach—Statistical Analysis: Cell viability and synergy calculations were calculated using three biological replicates. Cell viability and cell growth were normalized to the negative control (untreated cells that receive saline). Synergy calculations and statistical significance were determined using COMBENEFIT software.

In pharmacokinetic studies, statistical significance of tumor distribution data was determined by using one way analysis of variance (ANOVA) in Graphpad prism (GraphPad 5.0 Software, Inc., La Jolla, CA, USA). All data were expressed as mean ± standard deviation (SD) (n = 3). Differences between groups were determined by Tukey's multiple comparison test. Asterisks denote statistically significant differences (*$p < 0.05$; **$p < 0.01$; ***$p < 0.001$).

In in vivo tumor regression studies, statistical significance of tumor volume and tumor weight were evaluated by using one way ANOVA in Graphpad prism (GraphPad 5.0 Software, Inc., La Jolla, CA, USA). All data were expressed as mean ± standard deviation (n = 6). Differences between groups were determined by Tukey's multiple comparison test. Asterisks denote statistically significant differences (*$p < 0.05$; **$p < 0.01$; ***$p < 0.001$).

Survival data were generated by the Kaplan–Meier method, median survival and statistical significance were determined by log-rank test and Mann–Whitney U test, respectively. All data were expressed as mean ± standard deviation (n = 6). The statistical analysis of data was carried out using Graph pad prism 5.0 software (GraphPad PRISM, San Diego, CA, USA). Asterisks denote statistically significant differences (*$p < 0.05$; **$p < 0.01$; ***$p < 0.001$).

Supporting Information

Supporting information is available from the Wiley online library or from the author.

Conflict of Interest

The authors declare no conflict of interest.

[1] a) A. Kreso, C. A. O'Brien, P. van Galen, O. I. Gan, F. Notta, A. M. Brown, K. Ng, J. Ma, E. Wienholds, C. Dunant, A. Pollett, S. Gallinger, J. McPherson, C. G. Mulligan, D. Shibata, J. E. Dick, *Science* **2013**, *339*, 543; b) R. X. Zhang, H. L. Wong, H. Y. Xue, J. Y. Eoh, X. Y. Wu, *J. Controlled Release* **2016**, *240*, 489.

[2] a) C. E. Ashley, E. C. Carnes, G. K. Phillips, D. Padilla, P. N. Durfee, P. A. Brown, T. N. Hanna, J. Liu, B. Phillips, M. B. Carter, N. J. Carroll, X. Jiang, D. R. Dunphy, C. L. Willman, D. N. Petsev, D. G. Evans, A. N. Parikh, B. Chackerian, W. Wharton, D. S. Peabody, C. J. Brinker, *Nat. Mater.* **2011**, *10*, 389; b) Y. Chen, H. Chen, J. Shi, *Mol. Pharmaceutics* **2014**, *11*, 2495.

[3] a) A. Makkouk, G. J. Weiner, *Cancer Res.* **2015**, *75*, 5; b) T. Yin, L. Wang, L. Yin, J. Zhou, M. Huo, *Biomaterials* **2015**, *61*, 10; c) K. M. Au, Y. Min, X. Tian, L. Zhang, V. Perello, J. M. Caster, A. Z. Wang, *ACS Nano* **2015**, *9*, 8976.

[4] a) L. M. Phan, S.-C. J. Yeung, M.-H. Lee, *Cancer Biol. Med.* **2014**, *11*, 1; b) D. Hanahan, R. A. Weinberg, *Cell* **2011**, *144*, 646; c) G. J. Yoshida, *J. Exp. Clin. Cancer Res.* **2015**, *34*, 111; d) M. A. Pierotti, F. Berrino, M. Gariboldi, C. Melani, A. Mogavero, T. Negri, P. Pasanisi, S. Pilotti, *Oncogene* **2013**, *32*, 1475.

[5] a) Y. K. Chae, A. Arya, M.-K. Malecek, D. S. Shin, B. Carneiro, S. Chandra, J. Kaplan, A. Kalyan, J. K. Altman, L. Platanias, F. Giles, *Oncotarget* **2016**, *7*, 40767; b) I. N. Alimova, B. Liu, Z. Fan, S. M. Edgerton, T. Dillon, S. E. Lind, A. D. Thor, *Cell Cycle* **2009**, *8*, 909; c) A. Sonnenblick, D. Agbor-Tarh, I. Bradbury, S. Di Cosimo, H. A. Azim, D. Fumagalli, S. Sarp, A. C. Wolff, M. Andersson, J. Kroep, T. Cufer, S. D. Simon, P. Salman, M. Toi, L. Harris, J. Gralow, M. Keane, A. Moreno-Aspitia, M. Piccart-Gebhart, E. de Azambuja, *J. Clin. Oncol.* **2017**, *35*, 1421.

[6] G. Zhou, R. Myers, Y. Li, Y. Chen, X. Shen, J. Fenyk-Melody, M. Wu, J. Ventre, T. Doebber, N. Fujii, N. Musi, M. F. Hirshman, L. J. Goodyear, D. E. Moller, *J. Clin. Invest.* **2001**, *108*, 1167.

[7] a) D. R. Morales, A. D. Morris, *Annu. Rev. Med.* **2015**, *66*, 17; b) R. Ramjeesingh, C. Orr, C. S. Bricks, W. M. Hopman, N. Hammad, *Curr. Oncol.* **2016**, *23*, e116.

[8] R. J. Dowling, S. Niraula, V. Stambolic, P. J. Goodwin, *J Mol. Endocrinol.* **2012**, *48*, 12.

[9] M. Peng, K. O. Darko, T. Tao, Y. Huang, Q. Su, C. He, T. Yin, Z. Liu, X. Yang, *Cancer Treat. Rev.* **2017**, *54*, 24.

[10] a) T. Hu, Y. M. Chung, M. Ma, J. Ma, J. S. Berek, M. C. T. Hu, *Sci. Rep.* **2014**, *4*, 5810; b) https://clinicaltrials.gov/ct2/show/NCT01528046, (accessed: March 2018).

[11] J. von Pawel, U. Gatzemeier, J. L. Pujol, L. Moreau, S. Bildat, M. Ranson, G. Richardson, C. Steppert, A. Riviere, I. Camlett, S. Lane, G. Ross, *J. Clin. Oncol.* **2001**, *19*, 1743.

[12] M. Rodriguez, P. G. Rose, *Gynecol. Oncol.* **2001**, *83*, 257.

[13] C. Oberhoff, D. G. Kieback, R. Wurstlein, H. Deertz, J. Sehouli, C. van Soest, J. Hilfrich, M. Mesrogli, G. von Minckwitz, H. J. Staab, A. E. Schindler, *Onkologie* **2001**, *24*, 256.

[14] A. Korfel, C. Oehm, J. von Pawel, U. Keppler, M. Deppermann, S. Kaubitsch, E. Thiel, *Eur. J. Cancer* **2002**, *38*, 1724.

[15] a) L. D. Mayer, T. O. Harasym, P. G. Tardi, N. L. Harasym, C. R. Shew, S. A. Johnstone, E. C. Ramsay, M. B. Bally, A. S. Janoff, *Mol. Cancer Ther.* **2006**, *5*, 1854; b) J. H. Lee, A. Nan, *J. Drug Delivery* **2012**, *2012*, 17; c) R. X. Zhang, P. Cai, T. Zhang, K. Chen, J. Li, J. Cheng, K. S. Pang, H. A. Adissu, A. M. Rauth, X. Y. Wu, *Nanomedicine* **2016**, *12*, 1279.

[16] a) F. Z. Dahmani, Y. Xiao, J. Zhang, Y. Yu, J. Zhou, J. Yao, *Adv. Healthcare Mater.* **2016**, *5*, 1447; b) D. Chen, Q. Tang, J. Zou, X. Yang, W. Huang, Q. Zhang, J. Shao, X. Dong, *Adv. Healthcare Mater.* **2018**, *15*, 201701272.

[17] B. Zhang, T. Wang, S. Yang, Y. Xiao, Y. Song, N. Zhang, S. Garg, *J. Controlled Release* **2016**, *238*, 10.

[18] S. Gadde, *MedChemComm* **2015**, *6*, 1916.

[19] Y. H. Song, E. Shin, H. Wang, J. Nolan, S. Low, D. Parsons, S. Zale, S. Ashton, M. Ashford, M. Ali, D. Thrasher, N. Boylan, G. Troiano, *J. Controlled Release* **2016**, *229*, 106.

[20] Z. Li, J. C. Barnes, A. Bosoy, J. F. Stoddart, J. I. Zink, *Chem. Soc. Rev.* **2012**, *41*, 2590.

[21] a) J. L. Vivero-Escoto, I. I. Slowing, B. G. Trewyn, V. S. Y. Lin, *Small* **2010**, *6*, 1952; b) H. Zhang, D. R. Dunphy, X. Jiang, H. Meng, B. Sun, D. Tarn, M. Xue, X. Wang, S. Lin, Z. Ji, R. Li, F. L. Garcia, J. Yang, M. L. Kirk, T. Xia, J. I. Zink, A. Nel, C. J. Brinker, *J. Am. Chem. Soc.* **2012**, *134*, 15790.

[22] a) K. S. Butler, P. N. Durfee, C. Theron, C. E. Ashley, E. C. Carnes, C. J. Brinker, *Small* **2016**, *12*, 2173; b) Y. He, Z. Su, L. Xue, H. Xu, C. Zhang, *J. Controlled Release* **2016**, *229*, 80; c) W.-H. Chen, G.-F. Luo, Q. Lei, F.-Y. Cao, J.-X. Fan, W.-X. Qiu, H.-Z. Jia, S. Hong, F. Fang, X. Zeng, R.-X. Zhuo, X.-Z. Zhang, *Biomaterials* **2016**, *76*, 87; d) Y. Chen, K. Ai, J. Liu, G. Sun, Q. Yin, L. Lu, *Biomaterials* **2015**, *60*, 111; e) X. Wu, Z. Wang, D. Zhu, S. Zong, L. Yang, Y. Zhong, Y. Cui, *ACS Appl. Mater. Interfaces* **2013**, *5*, 10895; f) P. N. Durfee, Y.-S. Lin, D. R. Dunphy, A. J. Muñiz, K. S. Butler, K. R. Humphrey, A. J. Lokke, J. O. Agola, S. S. Chou, I. M. Chen, W. Wharton, J. L. Townson, C. L. Willman, C. J. Brinker, *ACS Nano* **2016**, *10*, 8325; g) V. Cauda, H. Engelke, A. Sauer, D. Arcizet, C. Bräuchle, J. Rädler, T. Bein, *Nano Lett.* **2010**, *10*, 2484.

[23] Q. Yang, T. Zhang, C. Wang, J. Jiao, J. Li, Y. Deng, *Eur. J. Pharm. Biopharm.* **2014**, *88*, 737.

[24] H. Yu, Q. Wang, Y. Sun, M. Shen, H. Li, Y. Duan, *PLoS One* **2015**, *10*, e0116502.

[25] X. Liu, A. Situ, Y. Kang, K. R. Villabroza, Y. Liao, C. H. Chang, T. Donahue, A. E. Nel, H. Meng, *ACS Nano* **2016**, *10*, 2702.

[26] H. Meng, M. Wang, H. Liu, X. Liu, A. Situ, B. Wu, Z. Ji, C. H. Chang, A. E. Nel, *ACS Nano* **2015**, *9*, 3540.

[27] a) A. Verma, S. Sharma, P. K. Gupta, A. Singh, B. V. Teja, P. Dwivedi, G. K. Gupta, R. Trivedi, P. R. Mishra, *Acta Biomater.* **2016**, *31*, 288; b) S. B. Koh, A. Courtin, R. J. Boyce, R. G. Boyle, F. M. Richards, D. I. Jodrell, *Cancer Res.* **2015**, *75*, 3583.

[28] a) D. M. Jonker, S. A. Visser, P. H. van der Graaf, R. A. Voskuyl, M. Danhof, *Pharmacol. Ther.* **2005**, *106*, 1; b) J. B. Fitzgerald, B. Schoeberl, U. B. Nielsen, P. K. Sorger, *Nat. Chem. Biol.* **2006**, *2*, 458.

[29] M. Jurkiewicz, D. A. Averill-Bates, M. Marion, F. Denizeau, *Biochim. Biophys. Acta, Mol. Cell Res.* **2004**, *1693*, 15.

[30] Y. Feng, C. Ke, Q. Tang, H. Dong, X. Zheng, W. Lin, J. Ke, J. Huang, S. C. Yeung, H. Zhang, *Cell Death Dis.* **2014**, *5*, e1088.

[31] Y. Yu, Z.-H. Wang, L. Zhang, H.-J. Yao, Y. Zhang, R.-J. Li, R.-J. Ju, X.-X. Wang, J. Zhou, N. Li, W.-L. Lu, *Biomaterials* **2012**, *33*, 1808.

[32] X. Cai, X. Hu, X. Tan, W. Cheng, Q. Wang, X. Chen, Y. Guan, C. Chen, X. Jing, *PLoS One* **2015**, *10*, e0133349.

[33] T.-W. Kim, P.-W. Chung, V. S. Y. Lin, *Chem. Mater.* **2010**, *22*, 5093.